



## 5G Communication with a Heterogeneous, Agile Mobile network in the Pyeongchang Winter Olympic competition

Grant agreement n. 723247

# Deliverable 3.4 Algorithms for backhauling & fronthauling

<b>Date of Delivery:</b>	May 31st 2017
<b>Editor:</b>	Nicolas Cassiau (CEA)
<b>Associate Editors:</b>	
<b>Authors:</b>	Gosan Noh (ETRI), Bing Hui (ETRI), Junhyeong Kim (ETRI), Heesang Chung (ETRI), Ilgyu Kim (ETRI), Nicolas Cassiau (CEA), Giuseppe Destino (UOULU)
<b>Dissemination Level:</b>	PU
<b>Security:</b>	Public
<b>Status:</b>	Final
<b>Version:</b>	V1.1
<b>File Name:</b>	5GCHAMPION_D3.4_Final.pdf
<b>Work Package:</b>	WP3



**Title:** Deliverable 3.4: Algorithms for backhauling & fronthauling  
**Date:** 31-05-2017      **Status:** Final  
**Security:** PU      **Version:** v1.1

Modifications	Date	Version
Initial document	21-03-2017	v0.1
All technical contributions integrated	23-05-2017	v1.0
Final editing	31-05-2017	v1.1

### Abstract

This deliverable addresses objective O3.4 of WP3, “Develop robust signal processing technologies to support very high bit rate services in high mobility”. More specifically, as expected in Task 3.2, it studies (i) beamforming algorithm for the mmW backhaul/fronthaul transceiver, (ii) link level solutions for high spectral efficiency and (iii) signal transmission in highly time-variant channels. Objective (iii) is addressed in chapter 2 and 3 where several numerology and reference signals designs are assessed for the backhaul of high speed train. Chapter 4 concerns objective (ii); spatial multiplexing is proposed as a MIMO method for increasing the throughput of the highly time variant link between high speed train and fixed transmitters along the railway. Finally, beam alignment techniques are provided in chapter 5 for addressing objective (i). In this deliverable, the 28-30 GHz carrier frequency is considered, where an enormous amount of spectrum is available, allowing multi-Gbps data transmission required for providing high speed Internet access to hundreds of users inside, for example, a train running up to 500 km/h.

### Index terms

Millimeter-wave; time variant channel; Doppler; high-speed train; numerology design; reference signal design; spatial multiplexing; beam alignment; beamforming codebook.



---

**Title:** Deliverable 3.4: Algorithms for backhauling & fronthauling  
**Date:** 31-05-2017      **Status:** Final  
**Security:** PU      **Version:** v1.1

---

## Contents

<b>1</b>	<b>Introduction .....</b>	<b>7</b>
<b>2</b>	<b>Numerology design for high speed train .....</b>	<b>8</b>
2.1	<i>Introduction</i>	8
2.2	<i>System description</i>	8
2.3	<i>OFDM numerology design for HST</i>	10
2.4	<i>Simulation results</i>	13
2.5	<i>Summary</i>	17
<b>3</b>	<b>Reference signal design robust to very high speed .....</b>	<b>17</b>
3.1	<i>Introduction</i>	17
3.2	<i>System description</i>	17
3.3	<i>DMRS design for very high mobility</i>	20
3.4	<i>Simulation results</i>	23
3.5	<i>Summary</i>	27
<b>4</b>	<b>Spatial multiplexing for backhauling of HST .....</b>	<b>27</b>
4.1	<i>Scenario</i>	27
4.2	<i>Channel model</i>	28
4.3	<i>Doppler modeling and pre-compensation</i>	29
4.4	<i>MIMO schemes</i>	29
4.5	<i>Simulation results</i>	31
4.6	<i>Summary</i>	34
<b>5</b>	<b>Beam alignment techniques.....</b>	<b>34</b>
5.1	<i>Transceiver architecture and communication model</i>	35
5.2	<i>Beamforming codebook</i>	36
5.3	<i>RSS-based strategy for single-path alignment</i>	39
5.4	<i>Summary</i>	46
<b>6</b>	<b>Conclusion.....</b>	<b>47</b>
	<b>References .....</b>	<b>48</b>



---

**Title:** Deliverable 3.4: Algorithms for backhauling & fronthauling  
**Date:** 31-05-2017      **Status:** Final  
**Security:** PU      **Version:** v1.1

---

## List of Acronyms

3GPP	Third Generation Partnership Project
5G	Fifth Generation
BBU	Baseband Unit
BLAST	Bell Labs Layered Space Time
BLER	Block Error Rate
BRS	Beam Reference Signal
CDL	Clustered Delay Line
CMOS	Complementary Metal Oxide Semi-conductor
CP	Cyclic Prefix
CRS	Common Reference Signal
DFE	Digital Front End
DFT	Discrete Fourier Transform
DMRS	Demodulation Reference Signal
FFT	Fast Fourier Transform
HST	High Speed Train
ICI	InterCarrier Interference
LMMSE	Linear Minimum Mean Square Error
LOS	Line Of Sight
LS	Least Squares
LTE	Long Term Evolution
MCS	Modulation and Coding Scheme
MIMO	Multiple Input Multiple Output
mmW	millimeter wave
NLOS	Non Line Of Sight
NR	New Radio
OFDM	Orthogonal Frequency Division Multiplexing
PER	Packet Error Rate
PLL	Phase Locked Loop
PSD	Power Spectral Density
PSS	Primary Synchronization Signal
QAM	Quadrature Amplitude Modulation
QoS	Quality of Service
RB	Resource Block
RF	Radio Frequency
RMS	Root Mean Square
RRH	Remote Radio Head
RRU	Remote Radio Unit
RS	Reference Signal
RSS	Received Signal Strength
SF	Sub Frame
SM	Spatial Multiplexing
SNR	Signal to Noise Ratio
SSS	Secondary Synchronization Signal
TDL	Tapped Delay Line
TE	Terminal Equipment
TRP	Transmit Receive Point
TRU	Terminal Radio Unit

The information contained in this document is the property of the contractors. It cannot be reproduced or transmitted to thirds without the authorization of the contractors.



---

**Title:** Deliverable 3.4: Algorithms for backhauling & fronthauling  
**Date:** 31-05-2017      **Status:** Final  
**Security:** PU      **Version:** v1.1

---

TTI      Time Transmission Interval  
UE      User Equipment  
ULA      Uniform Linear Array  
URA      Uniform Rectangular Array  
URLLC      Ultra-Reliable Low Latency Communications  
V-BLAST      Vertical BLAST

## Table of Figures

Figure 1 Network model for the high speed train scenario ..... 8  
Figure 2 Examples of phase noise models for the carrier frequency of 30 GHz ..... 11  
Figure 3 BLER vs. SNR for different subcarrier spacing and MCSs (Speed: 100 km/h) ..... 13  
Figure 4 BLER vs. SNR for different subcarrier spacing and MCSs (Speed: 300 km/h) ..... 14  
Figure 5 BLER vs. SNR for different subcarrier spacing and MCSs (Speed: 500 km/h) ..... 14  
Figure 6 Spectrum efficiency vs. SNR for different subcarrier spacing and MCSs (Speed: 100 km/h)..... 15  
Figure 7 Spectrum efficiency vs. SNR for different subcarrier spacing and MCSs (Speed: 300 km/h)..... 16  
Figure 8 Spectrum efficiency vs. SNR for different subcarrier spacing and MCSs (Speed: 500 km/h)..... 16  
Figure 9 Antenna configuration: (a) rectangular panel array; (b) antenna element pattern.... 19  
Figure 10 Front-loaded DMRS patterns with different time-domain densities: (a) baseline front-loaded DMRS; (b) front-loaded DMRS with 2x time-domain density; (c) front-loaded DMRS with 4x time-domain density. .... 22  
Figure 11 DMRS patterns with reduced density in the frequency domain: (a) 4 DMRS subcarriers per RB; (b) 2 DMRS subcarriers per RB. .... 23  
Figure 12 BLER vs. SNR (dB) for different DMRS patterns (1 layer) ..... 24  
Figure 13 BLER vs. SNR (dB) for different DMRS patterns (2 layers)..... 25  
Figure 14 Spectral efficiency vs. SNR for different DMRS patterns (1 layer) ..... 26  
Figure 15 Spectral efficiency vs. SNR for different DMRS patterns (2 layers) ..... 26  
Figure 16. Side view and top view of the scenario..... 28  
Figure 17. Gain of transmit antenna array element 1 (shown at  $\{x,y,z\}=\{0,0,0\}$ ), in dBi ..... 29  
Figure 18. Assessment of optimal antenna spacing for Spatial Multiplexing ..... 31  
Figure 19. Assessment of optimal antenna spacing for Diversity ..... 31  
Figure 20. Packet Error rate of Spatial Multiplexing and Diversity Schemes with 0.03 % residual Doppler. Legend: see Table 5 ..... 32



---

**Title:** Deliverable 3.4: Algorithms for backhauling & fronthauling  
**Date:** 31-05-2017      **Status:** Final  
**Security:** PU      **Version:** v1.1

---

Figure 21. Throughput of Spatial Multiplexing and Diversity Schemes with 0.03 % residual Doppler. Legend: see Table 5 ..... 33

Figure 22. Packet Error rate of Spatial Multiplexing and Diversity Schemes with 0.06 % residual Doppler. Legend: see Table 5 ..... 33

Figure 23. Throughput of Spatial Multiplexing and Diversity Schemes with 0.06 % residual Doppler. Legend: see Table 5 ..... 34

Figure 24: Beamforming at the TRU and RRU ..... 35

Figure 25: Reference signal mapping. a) Localized frequency domain, b) Distributed frequency domain, c) Localized time domain and d) Distributed time domain ..... 36

Figure 26: DFT beamforming codebook ..... 37

Figure 27: Hierarchical beamforming codebook ..... 38

Figure 28: Hierarchical beamforming to maximize the number of active elements ..... 39

Figure 29: Training with exhaustive search..... 40

Figure 30: Optimum overhead with exhaustive search ..... 41

Figure 31 : Training with adaptive search ..... 42

Figure 32: Achievable rate as a function of the beamtraining periodicity (frame length) ..... 44

Figure 33 : Achievable rate as a function of the training time and SNR ..... 45

Figure 34 : Achievable rate as a function of the training time and location ..... 45



---

<b>Title:</b>	Deliverable 3.4: Algorithms for backhauling & fronthauling	
<b>Date:</b>	31-05-2017	<b>Status:</b> Final
<b>Security:</b> PU		<b>Version:</b> v1.1

---

## 1 Introduction

Millimeter-wave (mmW) communication is considered one of the key innovations of 5G, due to the large available bandwidth and potential to enable tens of Gbps data rate as well as massive MIMO and beamforming. However, many challenges for hardware implementation, signal processing and algorithms are still open, especially for a 28 GHz technology. The EU-KR H2020 5GCHAMPION project is one of the first research project delivering a prototype of mmW RF-transceiver at 28 GHz, which is integrated with pre-commercial 5G base-band and core networks components. This deliverable addresses objective O3.4 of WP3 of the 5GCHAMPION project, “Develop robust signal processing technologies to support very high bit rate services in high mobility”. More specifically, as expected in Task 3.2, it studies (i) beamforming algorithm for the mmW backhaul/fronthaul transceiver, (ii) link level solutions for high spectral efficiency and (iii) signal transmission in highly time-variant channels.

In order to achieve high spectral efficiency in a mmW-based very high mobility scenario such as high speed train (iii), some fundamental link-level solutions are investigated in chapters 2 and 3. First, numerology design is conducted to maximize the link performance such as spectral efficiency. The aim is to find the best OFDM parameter sets including subcarrier spacing, FFT size, CP length, and subframe length with the link-level evaluation in a high speed train environment. Then, reference signal design is carried out which specifies the densities and locations of the reference signal in the frequency- and time-domains. The proposed reference signal design sets are intended to support accurate channel estimation in a very high mobility environment up to 500 km/h while limiting reference signal overhead to an acceptable level.

In chapter 4, Spatial Multiplexing (SM) is considered for increasing the data throughput on the backhaul link of a high speed train (ii). SM is a MIMO technique that allows, under some conditions, to increase the throughput by a factor  $N_t$ , with  $N_t$  the number of transmit antennas. In this chapter, a channel model at 28 GHz is used including high Doppler due to the train motion. SM allows to use low order modulation, which is of interest in this high mobility context. The SM scheme is compared to a classical diversity scheme in terms of achievable throughput.

One big challenge addressed in the project, especially when considering hardware constraints, is the initial access procedure in which both transmitter and receiver need to discover via one or multiple directions (i) in order to, for instance, maximize the signal-to-noise ratio (SNR). In chapter 5, we investigate and compare different search strategies in terms of the effective data-rate (considering the overhead). More specifically, the study focused on localized time domain mapping of the reference signal and exhaustive and hierarchical search strategies were considered. An optimum length of the training time was found for the exhaustive search and, it was found that it depends on the periodicity of the alignment procedure as well as relative location of the devices. The training procedure based on adaptive search is, however, the best performing method. In fact, results showed that the longer the training is (i.e., the higher the hierarchical level is) the higher the rate is. This leads to the conclusion that hierarchical search is more time and rate efficient.



## 2 Numerology design for high speed train

### 2.1 Introduction

As one of the 5G deployment scenarios, the high speed train scenario aims at providing continuous coverage along the high speed train tracks using either 4 or 30 GHz frequency band [1]. For the 4 GHz band case, a direct access link between an eNodeB and a user equipment (UE) inside the train is established. For the 30 GHz band case, on the other hand, the access link for the UE is established through a relay deployed on top of the train carriage.

In this chapter, we focus on the high speed train scenario employing the 30 GHz carrier frequency, where an enormous amount of spectrum is available, allowing multi-Gbps data transmission required for providing high speed Internet access to hundreds of users inside the train running up to 500km/h. In this high speed environment employing mmW band, the effects of Doppler shift/spread and phase noise become quite significant and should be taken into account for numerology design. Therefore, we propose the 3GPP 5G NR numerology parameters including subcarrier spacing, CP length, FFT size, subframe length, and so on. The numerology design aims to support scalability, making it also applicable to other use cases and deployment scenarios. We then evaluate the link-level performance such as block error rate (BLER) and spectrum efficiency through extensive simulations.

### 2.2 System description

#### 2.2.1 Network model

As depicted in Figure 1, we assume a straight line eNodeB placement along the rail track, where remote radio heads (RRHs) connected to the centralized baseband unit (BBU) pool are deployed along the railway. Each RRH is equipped with an antenna array which can create a directional narrow beam along with the track so as to guarantee continuous coverage along the track. Similarly, an antenna array is mounted on top of a train, generating a directional beam towards the RRH. The distance between the RRH and railway is assumed to be short (around 5m) as described in [2]. Since the additional gain of the beam steering is not significant in this scenario, we assume a fixed and uni-directional beamforming throughout this chapter.

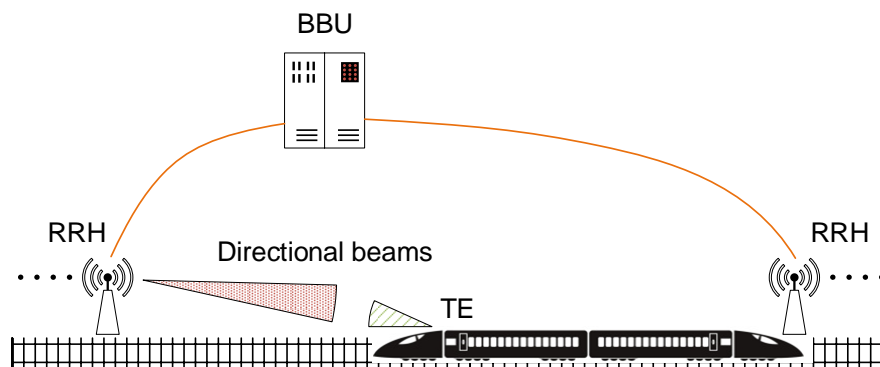


*Figure 1 Network model for the high speed train scenario*



---

**Title:** Deliverable 3.4: Algorithms for backhauling & fronthauling  
**Date:** 31-05-2017      **Status:** Final  
**Security:** PU      **Version:** v1.1

---

The UEs inside the train are assumed to communicate with the access points (APs) installed in each train carriage. The APs are connected to the terminal equipment (TE) deployed at the head of the train and relay user data streams between the RRHs and UEs. The link between the AP and UEs can be established via WiFi or femto cells which typically uses below 6 GHz band [3]. Inside the train carriage, the radio characteristics are similar to those of an indoor environment, and the transmission is done independently of the link between the RRH and the TE which uses around 30 GHz mmW band. Hence, we focus on the RRH-TE link rather than the AP-UE link.

### 2.2.2 Channel model

As mentioned above, around 30 GHz frequency band is assumed for the RRH-TE link. Combined with the directional beamforming scheme, mmW signals tend to propagate straightforwardly, which is quite different from the conventional below 6 GHz frequency band signals. The consequence of this is the line-of-sight (LOS)-dominant propagation where non-LOS (NLOS) components are rapidly attenuated. According to measurement campaigns carried out in New York City, it was shown that mmW channel has only two or three clusters and few tens of root mean square (RMS) delay spreads [4], [5].

In order to take these characteristics of the mmW propagation into account, the 3GPP has developed a new channel model for frequency spectrum above 6 GHz [6]. Since we are interested in the numerology design and the corresponding link-level evaluation, tapped delay line (TDL) models are used. Among the five TDL models, TDL-D model is selected for the evaluation of the 3GPP 5G NR high speed train scenario [2], where the Rician K-factor is 13.3 dB and the scaling of delay spread is 10 ns. The power delay profile of the selected TDL-D model is given in Table 1. It is clear that the LOS path dominates the channel power.

*Table 1 Power delay profile of TDL-D model with scaling of delay spread of 10 ns*

Tap #	Delay (ns)	Power (dB)	Fading distribution
1	0.00	-0.2	Rice, K = 13.3 dB
	0.00	-13.5	Rayleigh
2	0.35	-18.8	Rayleigh
3	6.12	-21	Rayleigh
4	13.63	-22.8	Rayleigh
5	14.05	-17.9	Rayleigh
6	18.04	-20.1	Rayleigh
7	25.96	-21.9	Rayleigh
8	17.75	-22.9	Rayleigh
9	40.42	-27.8	Rayleigh
10	79.37	-23.6	Rayleigh
11	94.24	-24.8	Rayleigh
12	97.08	-30.0	Rayleigh
13	125.25	-27.7	Rayleigh



---

<b>Title:</b>	Deliverable 3.4: Algorithms for backhauling & fronthauling	
<b>Date:</b>	31-05-2017	<b>Status:</b> Final
<b>Security:</b> PU		<b>Version:</b> v1.1

---

## 2.3 OFDM numerology design for HST

### 2.3.1 Effect of Doppler shift/spread

The mobility requirement of the 5G NR is 500 km/h [1]. In order to guarantee the quality-of-service (QoS) at that speed, the effects of Doppler shift and spread should be considered. In the TDL-D model we described above, the signal propagating through the LOS path experiences Doppler shift while those propagating through the NLOS paths experience Doppler spread caused by Rayleigh scattering. Hence, a combination of Doppler shift and spread affects the link-level performances such as BLER and spectrum efficiency. While the frequency offset due to the Doppler shift can be easily corrected by performing frequency offset compensation at a receiver, the effect of Doppler spread cannot be easily resolved. More specifically, if the channel varies within one OFDM symbol duration due to the reduced channel coherence time (i.e., the time duration during which the channel is considered invariant), the orthogonality among the subcarriers will be destroyed leading to intercarrier interference (ICI).

It is known that the channel coherence time is inversely proportional to Doppler spread of the channel [7]. Moreover, the maximum Doppler shift is proportional to the carrier frequency [8]. Therefore, the degradation due to the Doppler shift/spread becomes more significant when higher frequency bands such as mmW bands are used in addition to higher mobility. Hence, it is important to find the suitable OFDM numerology parameters such as the subcarrier spacing and the corresponding OFDM symbol and CP durations.

### 2.3.2 Effect of phase noise

Oscillators used to up- or down-convert signals in the transmitters or receivers are subject to phase noise. An ideal oscillator is expected to have an impulse in the spectrum at the oscillation frequency. However, the spectrum of a practical oscillator tends to disperse from the impulse due to phase noise. Phase noise causes two types of effects on the received OFDM signal: common phase error and ICI [9]. The common phase error is equally added to every subcarrier within an OFDM symbol duration, resulting in a rotation of the entire constellation. Hence, the amount of common phase error can be estimated and compensated at the receiver. Oppositely, the ICI exhibits AWGN-like behavior on the constellation which cannot be corrected or compensated.

The effect of phase noise is more significant for higher frequency bands such as mmW bands compared with the lower frequency bands. It is quite challenging to implement an RF oscillator with low phase noise characteristics in mmW bands [10]. Yet, the performance degradation due to the phase noise can be alleviated by using larger subcarrier spacing [9]. Hence, the effect of phase noise should be considered in the determination of the subcarrier spacing.

The phase noise can be characterized by the single-sided phase noise power spectral density (PSD) in unit of dBc/Hz. The modeling of phase noise is device-specific and faces a trade-off between performance and implementation complexity. In this regard, several phase noise models were proposed in the 3GPP 5G NR study, and some of them were agreed to be used in the 5G system design and evaluation [11]. Figure 2 shows the examples of phase noise models for the carrier frequency of 30 GHz. The phase locked loop (PLL)-based model characterizes phase noise parameters of CMOS-based RF chain for UE and GaAs-based RF chain for eNodeB [12]. The multi-pole/zero model uses three poles and zeros to model practical oscillators [13]. The mmMagic model is also PLL-based but uses different RF parameters [14].

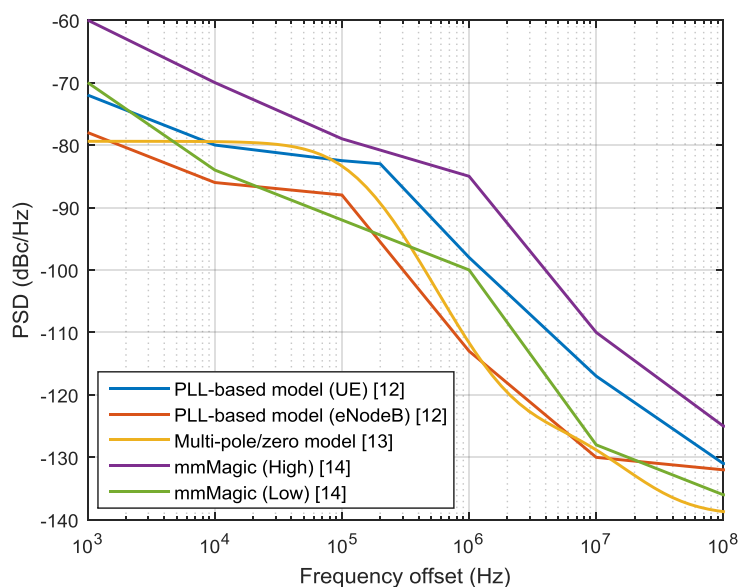


**Figure 2** Examples of phase noise models for the carrier frequency of 30 GHz

### 2.3.3 Proposed candidates of OFDM numerology

Considering the above effects of Doppler shift/spread and phase noise, we propose possible candidates of OFDM numerology parameters which satisfy the numerology scalability requirements in the 5G NR. Among these numerology candidates, one or multiple numerology sets are selected to support one or multiple UEs having the same or different propagation and RF transceiver characteristics such as carrier frequency, fading statistics, mobility, and RF impairment models.

#### 2.3.3.1 Candidates of subcarrier spacing

For the subcarrier spacing determination in the 5G NR, the following working assumptions were made on the 3GPP RAN1#85 meeting in May 2016 [15], i.e., a baseline subcarrier spacing of 15 kHz and a scaling factor of  $2^n$  with an integer  $n$ . The reason of making these working assumptions lies on the need for the efficient interworking with the LTE and the support of the subframe and/or slot boundary alignment among the numerology sets, respectively. Following to these working assumptions, the need for the scalability of subcarrier spacing up to 480 kHz (i.e.,  $n = 5$ ) is agreed on the 3GPP RAN1#86 meeting in August 2016. Hence, we consider the following scalable subcarrier spacing sets: {15, 30, 60, 120, 240, 480} kHz.

#### 2.3.3.2 Determination of fundamental OFDM parameters

The system bandwidth for the given 30 GHz carrier frequency is set as 80 MHz [2], which is quite larger than that of LTE having 20 MHz. In accordance with the scalable subcarrier spacing, we let the FFT size be scalable from 8192 (for the 15 kHz subcarrier spacing) to 256 (for the 480 kHz subcarrier spacing). By doing so, we can keep the same time-domain sampling rate among the numerology sets. In addition, assuming 10% guard band on the edges, the number



**Title:** Deliverable 3.4: Algorithms for backhauling & fronthauling  
**Date:** 31-05-2017 **Status:** Final  
**Security:** PU **Version:** v1.1

of used subcarriers are set to be also scalable from 4800 to 150. The corresponding OFDM symbol lengths are from 66.67  $\mu$ s to 2.08  $\mu$ s.

### 2.3.3.3 Determination of CP length

The CP length of each numerology candidate is set as the same ratio as that of the LTE, i.e., 7.8% for the first OFDM symbol and 7.0% for the other OFDM symbols. This easily enables the above mentioned 5G NR-LTE interworking and subframe/slot boundary alignment. Note that although the CP overhead is maintained, the CP length is reduced as the subcarrier spacing becomes larger. This tendency can be related to the shortened cell radius and reduced delay spread by the use of higher frequency bands and directional antenna where larger subcarrier spacing is required.

### 2.3.3.4 Determination of subframe length

The subframe length or a unit of transmission time interval (TTI) consists of 14 OFDM symbols as in the LTE. Hence, the subframe length is scaled down from 1000  $\mu$ s to 31.25  $\mu$ s as the subcarrier spacing scales up from 15 kHz to 480 kHz. It is expected that the Ultra-Reliable Low Latency Communication (URLLC) UEs are likely to use larger subcarrier spacing thereby satisfying fast scheduling and latency reduction requirements with the help of shortened TTI.

The above explained OFDM numerology parameters for the 5G NR are summarized in Table 2.

*Table 2 Proposed OFDM numerology parameter sets*

	Set 1	Set 2	Set 3	Set 4	Set 5	Set 6
<b>Subcarrier spacing (kHz)</b>	15	30	60	120	240	480
<b>System bandwidth (MHz)</b>	80	80	80	80	80	80
<b>FFT size</b>	8192	4096	2048	1024	512	256
<b>Sampling rate (MHz)</b>	122.88	122.88	122.88	122.88	122.88	122.88
<b>Number of used subcarriers</b>	4800	2400	1200	600	300	150
<b>OFDM symbol length (<math>\mu</math>s)</b>	66.67	33.33	16.67	8.33	4.17	2.08
<b>CP length of the 1<sup>st</sup> symbol (<math>\mu</math>s)</b>	6.05	3.08	1.54	0.82	0.46	0.28
<b>CP length of the remaining symbols (<math>\mu</math>s)</b>	4.66	2.33	1.16	0.58	0.28	0.14
<b>Number of symbols per subframe</b>	14	14	14	14	14	14
<b>Subframe length (<math>\mu</math>s)</b>	1000	500	250	125	62.5	31.25



## 2.4 Simulation results

### 2.4.1 BLER results

The BLER is defined as the ratio of the unsuccessfully decoded transport blocks to the total number of received transport blocks. We plotted the BLER as a function of SNR for different subcarrier spacing ( $\Delta f$ ) and MCS sets at the train speeds of 100, 300, and 500 km/h in Figure 3, Figure 4, and Figure 5, respectively.

As expected, it can be seen that the BLER is decreased when the SNR becomes higher but is increased when the higher modulation and coding rate are used. Also, we can see that the higher BLER is observed as the train runs faster, which is a direct result of the reduced channel coherence time and the corresponding Doppler-induced ICI.

In addition, it is shown that the BLER is remarkably degraded for shorter subcarrier spacing such as  $\Delta f = 15$  kHz and  $\Delta f = 30$  kHz, especially for higher MCSs and faster train speeds. In an extreme environment such as 256QAM with code rate 3/4 and 500 km/h train speed, only subcarrier spacing values larger than 120 kHz will result in satisfactory BLER performances. In addition to the enhanced immunity to the Doppler shift/spread, the use of larger subcarrier spacing is more robust against the effect of phase noise in a high speed and high carrier frequency environment.

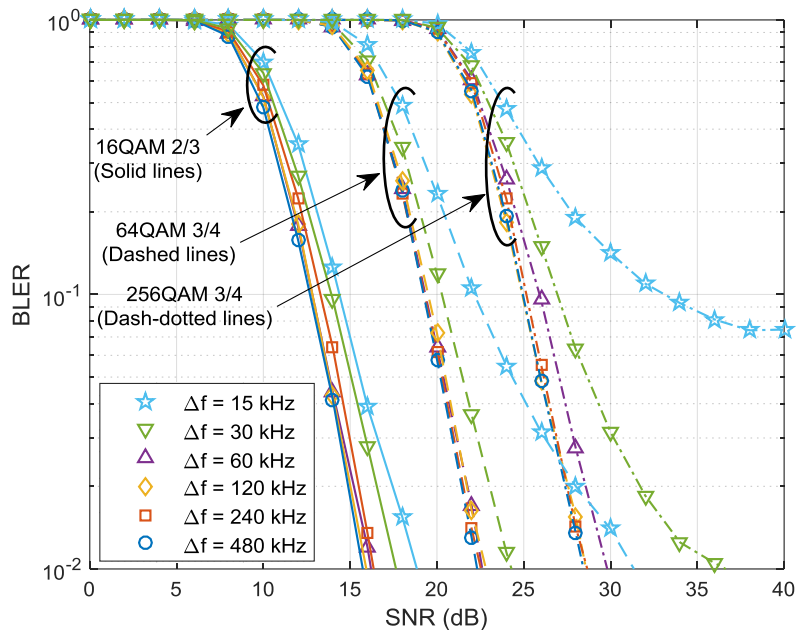


**Figure 3** BLER vs. SNR for different subcarrier spacing and MCSs (Speed: 100 km/h)

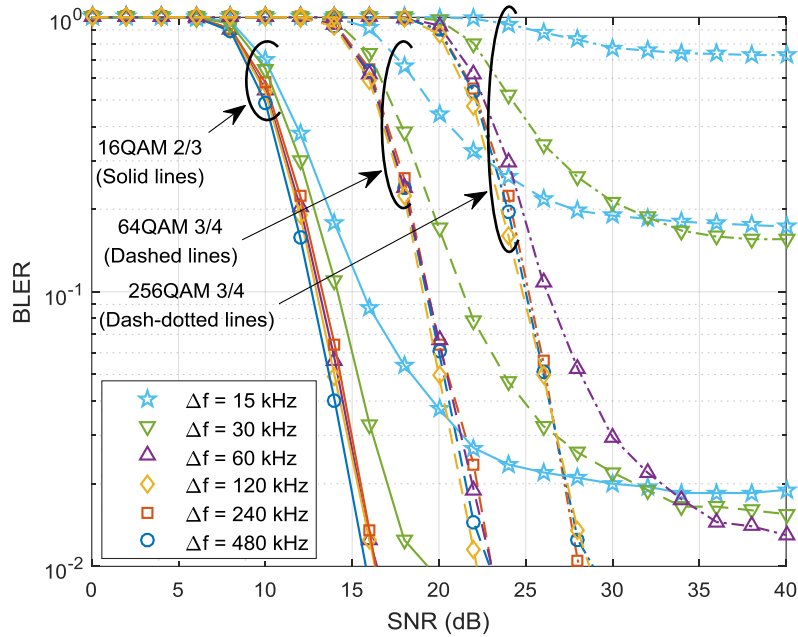


Figure 4 BLER vs. SNR for different subcarrier spacing and MCSs (Speed: 300 km/h)

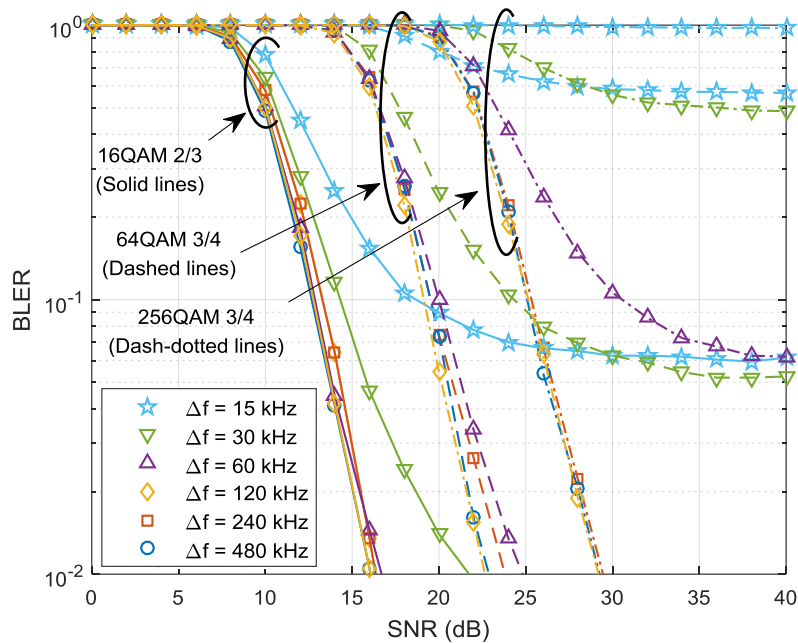


Figure 5 BLER vs. SNR for different subcarrier spacing and MCSs (Speed: 500 km/h)



### 2.4.2 Spectrum efficiency results

The spectrum efficiency is defined as the number of correctly received information bits in a given period of time and within a given bandwidth, which can be calculated as

$$\eta = \frac{(1 - \text{BLER})K}{\text{TTI} \cdot \omega}$$

where  $K$  denotes the transport block size and  $\omega$  represents the system bandwidth [2].

The spectrum efficiency provides a measure of how the proposed numerology helps to efficiently utilize the available bandwidth. We plotted the spectrum efficiency as a function of SNR for different subcarrier spacings and MCS sets at the train speed of 100, 300, and 500 km/h on Figure 6, Figure 7, and Figure 8, respectively.

Overall, the performance trend is similar to that of BLER. The spectrum efficiency is degraded with higher train speed, shorter subcarrier spacing, and higher MCS set. It can be seen that the use of large subcarrier spacing ( $\geq 120$  kHz) ensures satisfactory spectrum efficiency performance in most cases.

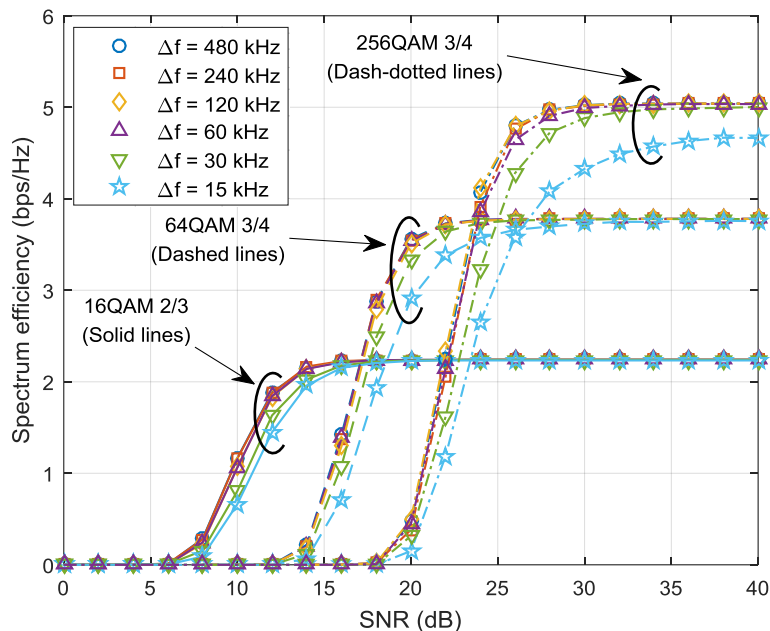


**Figure 6** Spectrum efficiency vs. SNR for different subcarrier spacing and MCSs (Speed: 100 km/h)

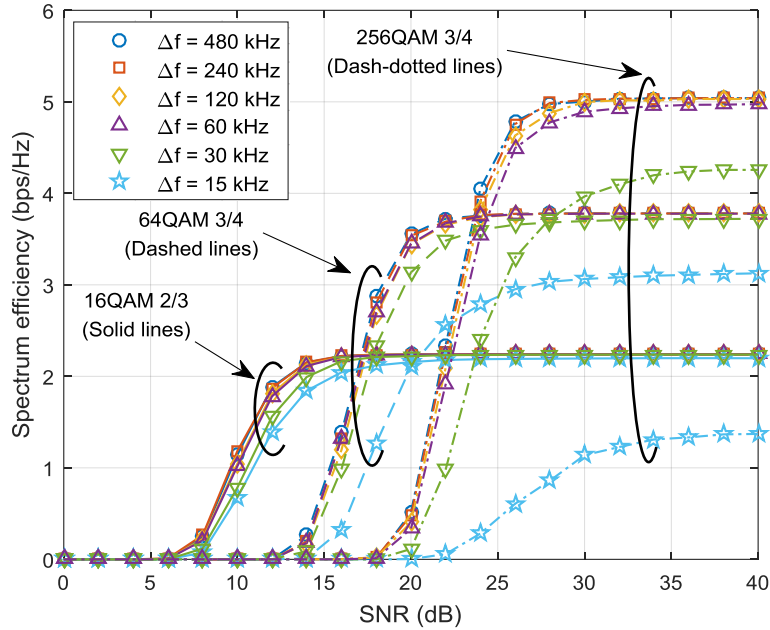


Figure 7 Spectrum efficiency vs. SNR for different subcarrier spacing and MCSs (Speed: 300 km/h)

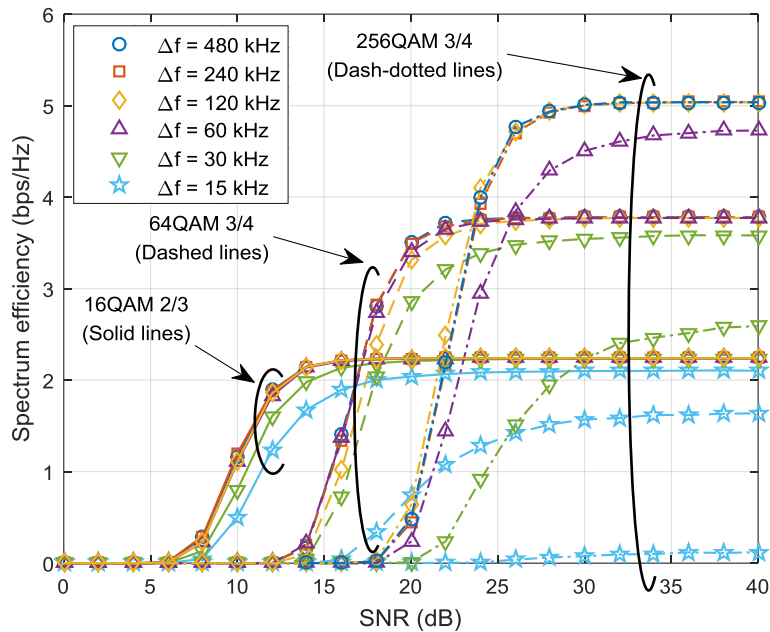


Figure 8 Spectrum efficiency vs. SNR for different subcarrier spacing and MCSs (Speed: 500 km/h)



---

<b>Title:</b>	Deliverable 3.4: Algorithms for backhauling & fronthauling	
<b>Date:</b>	31-05-2017	<b>Status:</b> Final
<b>Security:</b> PU		<b>Version:</b> v1.1

---

## 2.5 Summary

In this chapter, we proposed possible 3GPP 5G NR numerology sets including subcarrier spacing, CP length, FFT size, subframe length, and so on in a 30 GHz carrier frequency band. The OFDM numerology parameters are designed to provide scalability and consider Doppler and phase noise effects that have significant impact on the mmW system performance. We then evaluated the BLER and spectrum efficiency of the proposed numerology sets through extensive link-level simulations. In a high speed train environment, we found that using larger subcarrier spacing values of at least 120kHz would be beneficial in terms of BLER and spectrum efficiency performances.

## 3 Reference signal design robust to very high speed

### 3.1 Introduction

In the high speed environment employing mmW band, the effects of Doppler shift/spread become quite significant and should be taken into account for demodulation reference signal (DMRS) design for channel estimation. Since the 5G NR strives to adopt user-specific DMRS structure instead of common reference signal (CRS) structure, DMRS patterns tailored to the high speed UE can be used.

Therefore, in this chapter, we propose possible DMRS patterns suitable for the 3GPP 5G NR high speed train scenario and provide performance comparison among them through extensive link-level simulations. Considering the carrier frequency of 30 GHz, each DMRS design specifies density and location of the DMRS symbols in the frequency- and time-domains. The DMRS design aims to find the best trade-off between the channel estimation accuracy improvement and DMRS overhead reduction. The proposed DMRS patterns and their simulation results will not be restricted only to the high speed train scenario, but will also be useful to other deployment scenarios with high mobility.

### 3.2 System description

#### 3.2.1 Network model

We assume a straight line base station deployment along the rail track, where remote radio heads (RRHs) connected to the centralized baseband unit (BBU) pool are deployed along the railway. Each RRH is equipped with an antenna array which can create a directional narrow beam along the track so as to guarantee continuous coverage along the track. Similarly, an antenna array is mounted on top of a train, generating a directional beam towards the RRH. We assume a fixed and uni-directional beamforming.

The UEs inside the train are assumed to communicate with the access points (APs) installed in each train carriage. The link between the AP and UEs can be established via WiFi or femto cells [3]. Inside the train carriage, the radio characteristics are similar to those of an indoor environment, and the transmission is done independently of the link between the RRH and the onboard relay. Hence, we focus on the link between the RRH and onboard relay rather than on the link between the AP and UEs.



---

<b>Title:</b>	Deliverable 3.4: Algorithms for backhauling & fronthauling	
<b>Date:</b>	31-05-2017	<b>Status:</b> Final
<b>Security:</b> PU		<b>Version:</b> v1.1

---

### 3.2.2 Antenna configuration

A uniform rectangular panel array antenna is assumed for both the RRH and train onboard relay. Antenna elements are uniformly placed on the two-dimensional antenna panel [6], as illustrated in Figure 9a. Antenna configuration parameters are as follows:

- $M$ : the number of antenna elements in the vertical direction
- $N$ : the number of antenna elements in the horizontal direction
- $d_V$ : antenna spacing in the vertical direction
- $d_H$ : antenna spacing in the horizontal direction
- $P$ : antenna polarization types, i.e., single polarization ( $P = 1$ ) or dual polarization ( $P = 2$ )

The 3D radiation pattern for each antenna element  $A''(\theta'', \phi'')$  can be described as functions of the zenith angle  $\theta''$  and the azimuth angle  $\phi''$  as defined in [6], reproduced below:

$$A''(\theta'', \phi'') = -\min\{-[A_{E,V}(\theta'') + A_{E,H}(\phi'')], A_m\}$$

where the vertical radiation pattern  $A_{E,V}(\theta'')$  and the horizontal radiation pattern  $A_{E,H}(\phi'')$  are given by

$$A_{E,V}(\theta'') = -\min\left\{12\left(\frac{\theta'' - 90^\circ}{\theta_{3\text{dB}}}\right)^2, SLA_V\right\}, \theta_{3\text{dB}} = 65^\circ, SLA_V = 30\text{ dB}$$

$$A_{E,H}(\phi'') = -\min\left\{12\left(\frac{\phi''}{\phi_{3\text{dB}}}\right)^2, A_m\right\}, \phi_{3\text{dB}} = 65^\circ, A_m = 30\text{ dB}$$

The antenna element pattern is illustrated in Figure 9b.

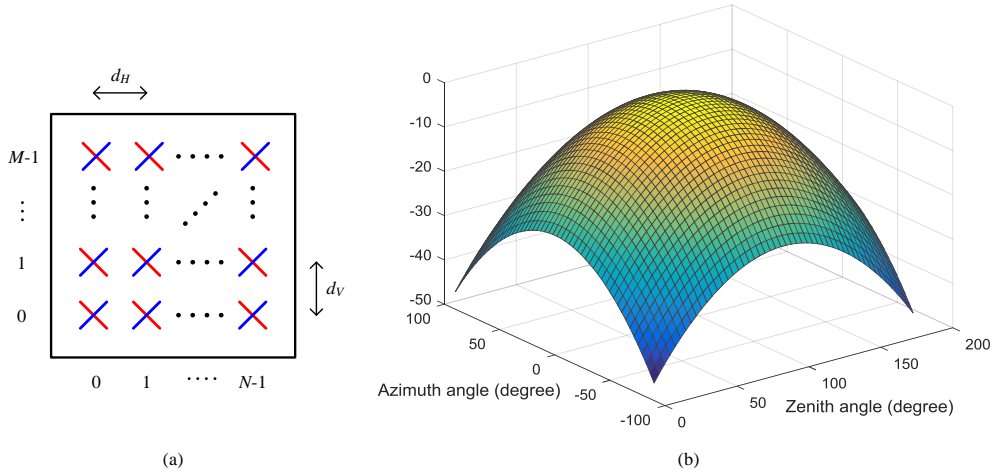


**Figure 9 Antenna configuration: (a) rectangular panel array; (b) antenna element pattern**

### 3.2.3 Channel model

In order to take mmW propagation characteristics into account, 3GPP has developed a new channel model for the frequency band above 6 GHz [6]. Since we are focusing on the DMRS design and the corresponding link-level evaluation in a multi-antenna configuration, clustered delay line (CDL) model is used. Among the five CDL models, CDL-D model is agreed for the DMRS evaluation of the 3GPP 5G NR high speed train scenario [2], where the Rician K-factor is 13.3 dB and the scaling of delay spread is 10 ns. The power delay profile of the selected CDL-D model is given in Table I. It is clear that the LOS path dominates the channel power. The following angular spread values are considered: azimuth spread of departure angle (ASD), azimuth spread of arrival angle (ASA), zenith spread of departure angle (ZSD), and zenith spread of arrival angle (ZSA). These angular spread values for high speed train scenario for within-cluster are given as  $c_{ASD} = c_{ASA} = 5^\circ$  and  $c_{ZSD} = c_{ZSA} = 1^\circ$  [16].

The channel coefficient generation of the CDL model consists the following steps [6]:

- Step 1: Departure and arrival angles generation according to the per-cluster departure and arrival angles and the ray offset angles within a cluster.
- Step 2: Coupling of departure and arrival rays within a cluster.
- Step 3: Cross-polarization power ratios generation for each ray.
- Step 4: Channel coefficient generation.

The channel coefficient  $H_{u,s}(\tau, t)$  between receive antenna  $u$  and transmit antenna  $s$  at time instance  $t$  and delay  $\tau$  is defined as

$$H_{u,s}(\tau, t) = \sqrt{\frac{1}{K+1}} \sum_{n=1}^N H_{u,s,n}^{NLOS}(t) \delta(\tau - \tau_n) + \sqrt{\frac{K}{K+1}} \sum_{n=1}^N H_{u,s,1}^{LOS}(t) \delta(\tau - \tau_n)$$



where  $K$  is the Rician  $K$ -factor in a linear scale and  $\tau_n$  is the delay of the  $n$ -th cluster.  $\delta(\cdot)$  is Dirac's delta function.

For each NLOS cluster,  $H_{u,s,n}^{\text{NLOS}}(t)$  is given by

$$H_{u,s,n}^{\text{NLOS}}(t) = \sqrt{\frac{P_n}{M}} \begin{bmatrix} F_{rx,u,\theta}(\theta_{n,m,ZOA}, \phi_{n,m,AOA}) \\ F_{rx,u,\phi}(\theta_{n,m,ZOA}, \phi_{n,m,AOA}) \end{bmatrix}^T \begin{bmatrix} \exp(j\Phi_{n,m}^{\theta\theta}) & \sqrt{\kappa_{n,m}^{-1}} \exp(j\Phi_{n,m}^{\theta\phi}) \\ \sqrt{\kappa_{n,m}^{-1}} \exp(j\Phi_{n,m}^{\phi\theta}) & \exp(j\Phi_{n,m}^{\phi\phi}) \end{bmatrix} \begin{bmatrix} F_{tx,s,\theta}(\theta_{n,m,ZOD}, \phi_{n,m,AOD}) \\ F_{tx,s,\phi}(\theta_{n,m,ZOD}, \phi_{n,m,AOD}) \end{bmatrix} \exp\left(\frac{j2\pi(\hat{r}_{rx,n,m}^T \bar{d}_{rx,u})}{\lambda_0}\right) \exp\left(\frac{j2\pi(\hat{r}_{tx,n,m}^T \bar{d}_{tx,s})}{\lambda_0}\right) \exp\left(j2\pi \frac{\hat{r}_{rx,n,m}^T \bar{v}}{\lambda_0} t\right)$$

where

- $P_n$ : the power of the  $n$ -th cluster in a linear scale
- $F_{rx,u,\theta}(\cdot, \cdot)$ ,  $F_{rx,u,\phi}(\cdot, \cdot)$ : the receive antenna radiation patterns in the direction of  $\theta$  and  $\phi$ , respectively
- $F_{tx,s,\theta}(\cdot, \cdot)$ ,  $F_{tx,s,\phi}(\cdot, \cdot)$ : the transmit antenna radiation patterns in the direction of  $\theta$  and  $\phi$ , respectively
- $\{\Phi_{n,m}^{\theta\theta}, \Phi_{n,m}^{\theta\phi}, \Phi_{n,m}^{\phi\theta}, \Phi_{n,m}^{\phi\phi}\}$ : set of random initial phases for four different polarization combinations, i.e.,  $\theta\theta$ ,  $\theta\phi$ ,  $\phi\theta$ , and  $\phi\phi$
- $\kappa_{n,m}$ : the cross polarization power ratio (XPR) for  $n$ -th cluster and  $m$ -th ray
- $\lambda_0$ : wavelength of the carrier frequency
- $\hat{r}_{rx,n,m}$ ,  $\hat{r}_{tx,n,m}$ : spherical unit vectors of receive and transmit antennas, respectively
- $\bar{d}_{rx,u}$ ,  $\bar{d}_{tx,s}$ : location vectors of receive and transmit antennas, respectively
- $\bar{v}$ : velocity vector

For the LOS path,  $H_{u,s,1}^{\text{NLOS}}(t)$  is given by

$$H_{u,s,1}^{\text{LOS}}(t) = \begin{bmatrix} F_{rx,u,\theta}(\theta_{LOS,ZOA}, \phi_{LOS,AOA}) \\ F_{rx,u,\phi}(\theta_{LOS,ZOA}, \phi_{LOS,AOA}) \end{bmatrix}^T \begin{bmatrix} \exp(j\Phi_{LOS}) & 0 \\ 0 & -\exp(j\Phi_{LOS}) \end{bmatrix} \begin{bmatrix} F_{tx,s,\theta}(\theta_{LOS,ZOD}, \phi_{LOS,AOD}) \\ F_{tx,s,\phi}(\theta_{LOS,ZOD}, \phi_{LOS,AOD}) \end{bmatrix} \cdot \exp\left(\frac{j2\pi(\hat{r}_{rx,LOS}^T \bar{d}_{rx,u})}{\lambda_0}\right) \cdot \exp\left(\frac{j2\pi(\hat{r}_{tx,LOS}^T \bar{d}_{tx,s})}{\lambda_0}\right) \cdot \exp\left(j2\pi \frac{\hat{r}_{rx,LOS}^T \bar{v}}{\lambda_0} t\right)$$

### 3.3 DMRS design for very high mobility

#### 3.3.1 DMRS design principle

The DMRS design is strongly related to the channel characteristics because the main purpose of DMRS is to estimate the channel coefficient for coherent detection. More specifically, if the channel fluctuates more severely in the frequency domain (i.e., having shorter channel coherence bandwidth), the DMRS density in the frequency-domain should be increased. Similarly, if the channel varies faster (i.e., having shorter channel coherence time), denser DMRS allocation in the time-domain is needed.

After determining frequency/time-domain DMRS densities, the DMRS locations in the time-frequency resource grid should be considered. Assuming stationary channel conditions,



---

<b>Title:</b>	Deliverable 3.4: Algorithms for backhauling & fronthauling	
<b>Date:</b>	31-05-2017	<b>Status:</b> Final
<b>Security:</b> PU		<b>Version:</b> v1.1

---

uniform DMRS allocation in both the frequency and time-domains is preferred for minimizing interpolation error and reducing implementation complexity.

Note that there is a tradeoff relationship between the channel estimation accuracy and DMRS overhead. Since any useful data cannot be transmitted by DMRS, allocating DMRS with a proper density is required for throughput maximization.

### 3.3.2 Front-loaded DMRS patterns with increased time-domain density

In NR, the baseline front-loaded DMRS structure is agreed due to its ability for achieving low latency [2]. In the time-frequency resource grid, the front-loaded DMRS can be located just after the control region, followed by data region, as seen in Figure 10a. As soon as obtaining channel estimates from the front-loaded DMRS, the receiver can demodulate data in the data region.

This front-loaded RS structure is particularly advantageous in decoding latency reduction for low mobility scenarios where channel coherence time is longer than the time period of front-loaded RSs. However, allocating only the frontloaded DMRS can degrade the link performance when the UE speed becomes higher (i.e., channel coherence time becomes shorter). Although the channel information in the data region can be obtained by interpolation, the channel information accuracy severely degrades with higher mobility. Hence, we consider the front-loaded DMRS patterns with 2x and 4x time-domain densities in Figure 10b and Figure 10c, respectively.

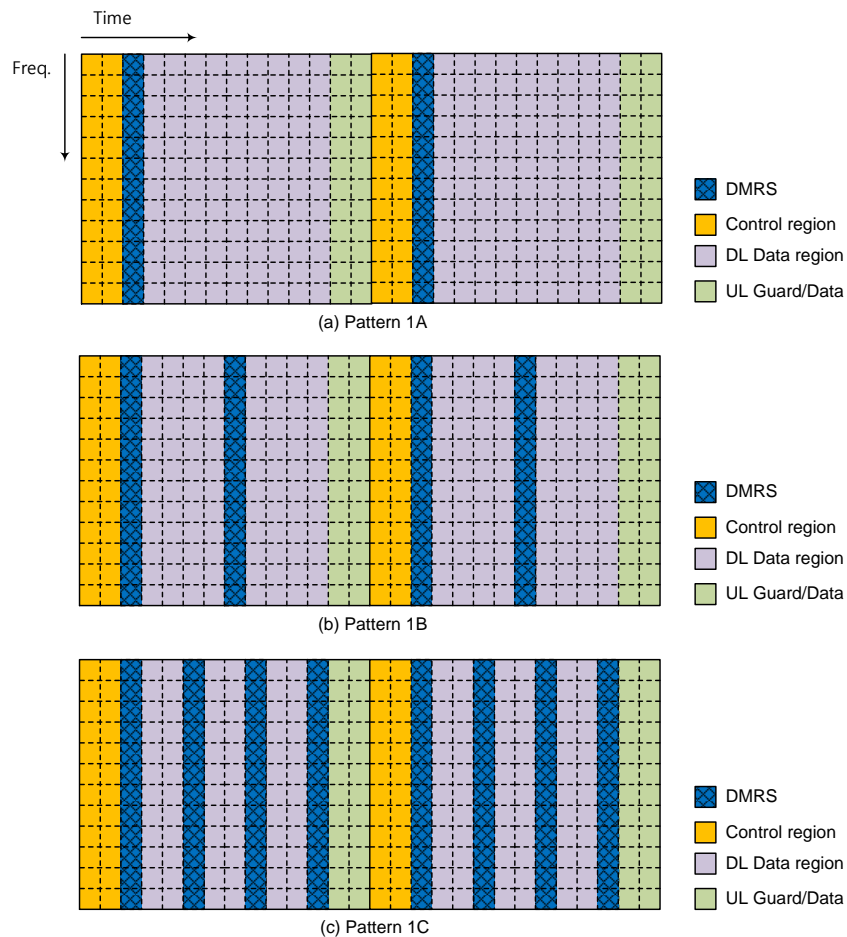


**Figure 10** Front-loaded DMRS patterns with different time-domain densities: (a) baseline front-loaded DMRS; (b) front-loaded DMRS with 2x time-domain density; (c) front-loaded DMRS with 4x time-domain density.

### 3.3.3 Reducing Frequency-Domain Density

Most high speed train tracks are quite straight, leading to a LOS-dominant channel condition. In this situation, the delay spread is expected to be shorter (or equivalently the channel coherence bandwidth becomes larger). Then, we can consider reducing frequency-domain density of the DMRS without significant degradation of channel estimation accuracy. By doing so, the overhead due to the DMRS can be much reduced. Examples of frequency-domain low-density DMRS patterns are given in Figure 11a (4 subcarriers per RB) and Figure 11b (2 subcarriers per RB), respectively. For MIMO transmission, up to 2 frequency-domain orthogonal DMRS ports are supported: Port 0 and Port 1.

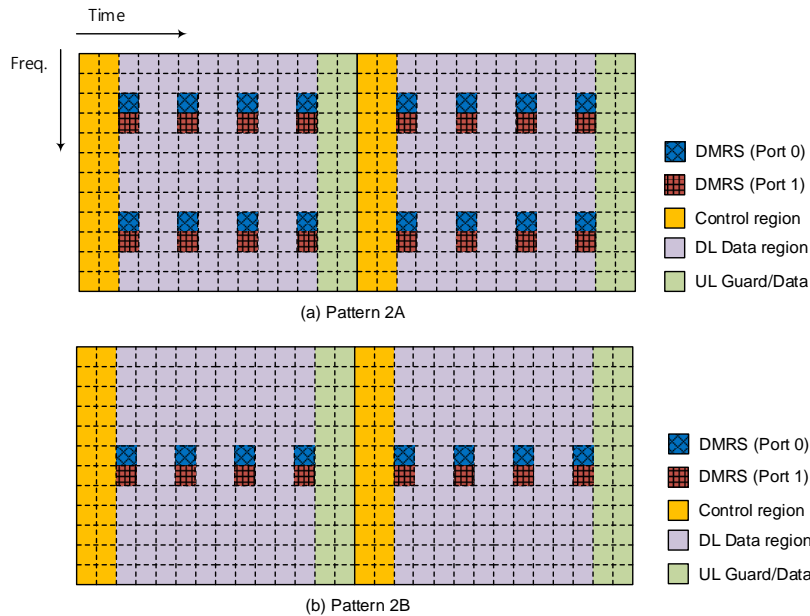


**Figure 11 DMRS patterns with reduced density in the frequency domain: (a) 4 DMRS subcarriers per RB; (b) 2 DMRS subcarriers per RB.**

### 3.4 Simulation results

We provide link-level simulation results in order to evaluate the proposed DMRS patterns in terms of BLER and spectrum efficiency. The simulation parameters are based on the high speed train scenario where the RRH-onboard relay link uses the mmW band. The detailed simulation parameters are summarized in Table 3.

**Table 3 Link-level simulation parameters**

Parameter	Value
Carrier frequency	30 GHz
System bandwidth	80 MHz
Subcarrier spacing	120 kHz
Channel coding	LTE Turbo
MCS	16QAM 3/4
Number of MIMO layers	1, 2
Channel estimation	LS estimation and linear interpolation
Equalizer	LMMSE
Channel model	<ul style="list-style-type: none"> <li>CDL-D (delay spread = 10 ns, K-factor = 13.3 dB)</li> <li>Parameter set # 1: 5(ASD), 5(ASA), 1(ZSA), 1(ZSD)</li> <li>ZoD and ZoA for cluster #1 are fixed at 90 degrees</li> </ul>
Transmit receive point (TRP) antenna configuration	<ul style="list-style-type: none"> <li>(M,N,P,Mg,Ng) = (8,8,2,1,1); (dV,dH) = (0.5, 0.5)<math>\lambda</math> with directional antenna element (HPBW=65°, directivity 8dB)</li> </ul>
UE antenna configuration	<ul style="list-style-type: none"> <li>(M,N,P,Mg,Ng) = (8,8,2,1,1); (dV,dH) = (0.5, 0.5)<math>\lambda</math> with directional antenna element (HPBW=65°, directivity 8dB)</li> </ul>
Phase noise model	Multi-pole/zero model [3]
UE speed	500 km/h

The information contained in this document is the property of the contractors. It cannot be reproduced or transmitted to thirds without the authorization of the contractors.



### 3.4.1 BLER results

We plotted the BLER as a function of SNR for different DMRS patterns in Figure 12 (1 Layer) and in Figure 13 (2 Layers). The BLER when having the ideal channel information is also plotted for comparison. As expected, it can be seen that the BLER is decreased when denser DMRS pattern is employed both in the time and frequency domains. Due to short coherence time, we need to have more than 4 DMRS within a slot in the time domain in order to satisfactorily support the UE speed of 500 km/h.

We also observe that reduced DMRS allocation in the frequency-domain does not significantly degrade BLER. This is because the employed CDL-D channel with delay spread 10 ns has strong LOS path and weaker multi-path components, making the channel coherence bandwidth quite large.

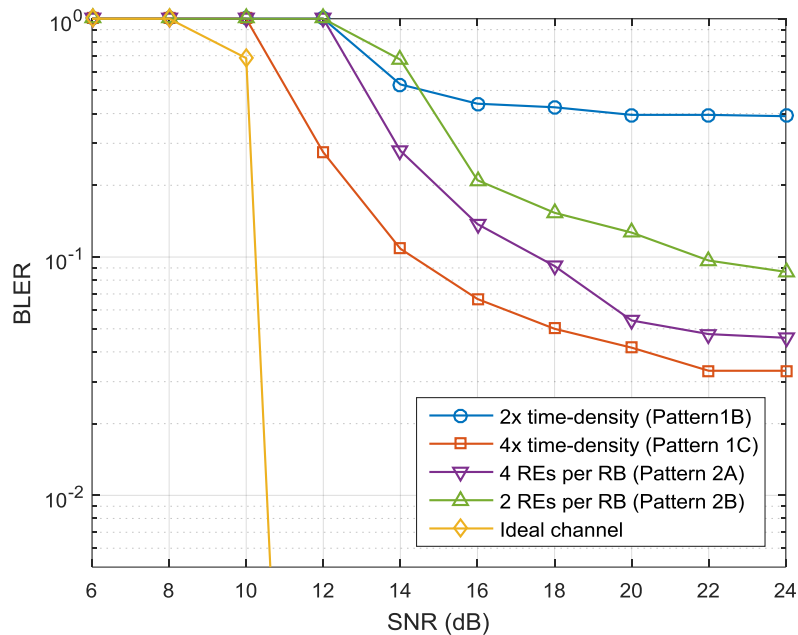


**Figure 12 BLER vs. SNR (dB) for different DMRS patterns (1 layer)**

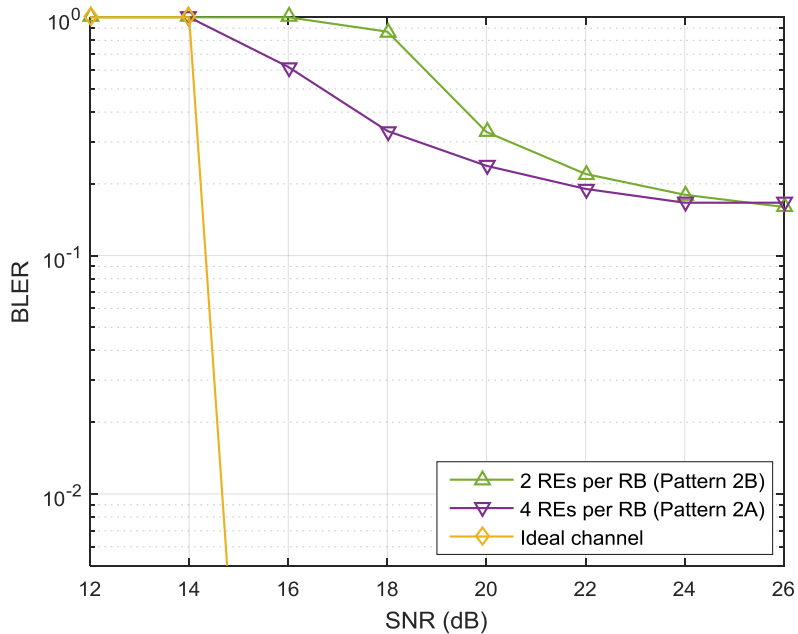


**Figure 13 BLER vs. SNR (dB) for different DMRS patterns (2 layers)**

### 3.4.2 Spectrum efficiency results

The spectrum efficiency provides a measure of how the proposed DMRS design helps efficiently utilize the available bandwidth. We plotted the spectral efficiency as a function of SNR for different DMRS patterns in Figure 14 (1 Layer) and in Figure 15 (2 Layers). Overall, the performance trend is similar to that of BLER. The spectral efficiency when the ideal channel information is available is also plotted for comparison. The spectral efficiency is degraded with less time-domain density DMRS.

The effect of reducing DMRS density in the frequency domain can be advantageous in enhancing spectral efficiency. For 1 layer case, reducing the DMRS density in the frequency domain less than 4 resource elements per RB is not beneficial to improve the spectral efficiency. However, for 2 layers case, 2 resource elements per RB provides higher spectral efficiency in the SNR region higher than 20 dB.

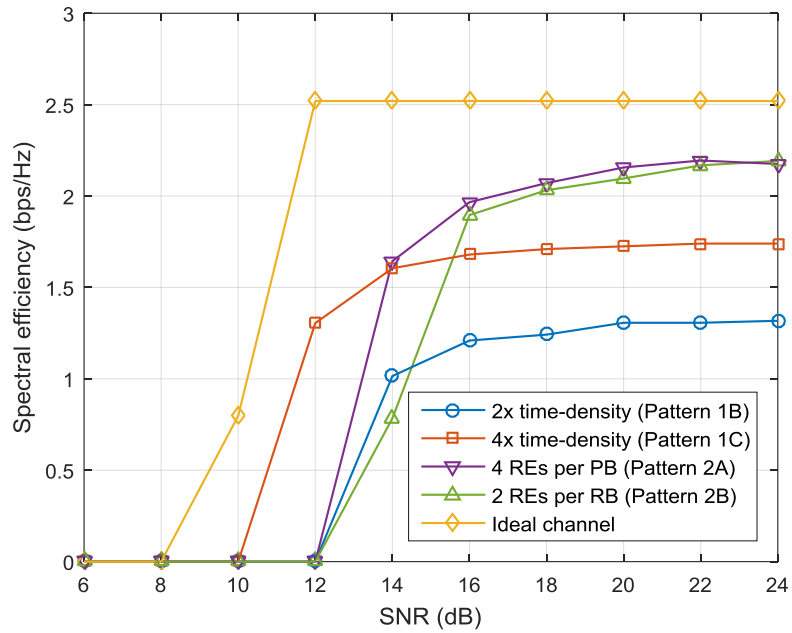


Figure 14 Spectral efficiency vs. SNR for different DMRS patterns (1 layer)

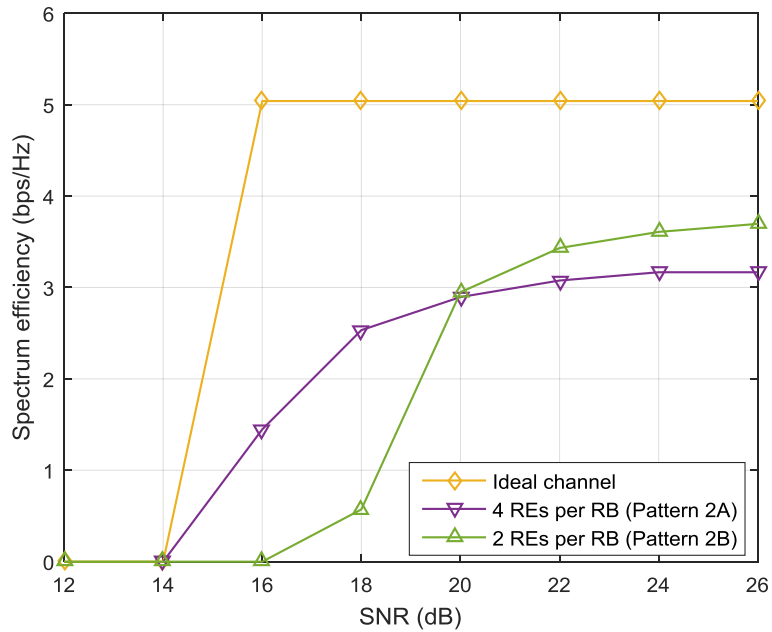


Figure 15 Spectral efficiency vs. SNR for different DMRS patterns (2 layers)



---

<b>Title:</b>	Deliverable 3.4: Algorithms for backhauling & fronthauling	
<b>Date:</b>	31-05-2017	<b>Status:</b> Final
<b>Security:</b> PU		<b>Version:</b> v1.1

---

### 3.5 Summary

We proposed possible candidates for the 3GPP 5G NR DMRS design in the 30 GHz carrier frequency band. The DMRS design is conducted so as to find the best tradeoff between the channel estimation accuracy improvement and overhead reduction, considering severe Doppler effect of the high speed train scenario. We then evaluated the BLER and spectrum efficiency of the proposed DMRS sets through extensive link-level simulations. We found that, in a high speed train environment, using frequency-domain sparse and time-domain dense DMRS allocation would be beneficial in terms of BLER and spectrum efficiency performances.

## 4 Spatial multiplexing for backhauling of HST

The study in [17] shows that there exists, under some conditions, a link with good SNR between a receiver on the top of a High Speed Train (HST) and a fixed Terminal Radio Unit (TRU) along the railway. Based on the results from this study, we assess here the possibility of using Multiple Input multiple Output (MIMO) schemes to enhance the throughput on this link, especially when Doppler is present. More particularly, Spatial Multiplexing (SM) [19] is assessed.

### 4.1 Scenario

We consider the backhauling of a HST; the scenario is illustrated on Figure 16. Our study is based on the results from [17], amongst which the following are of particular interest for us:

- *“It is possible to serve one train using two independant mmW links simultaneously”* (TRU1-RRU1 and TRU2-RRU2).
- The SNR of each link allows for MCSs up to 64-QAM, in a SISO mode.

We introduce multiple antennas at the TRU and the RRU side, see Figure 16 top view. We will focus, without loss of generality, on the TRU1-RRU1 link. We consider street canyon channel environment, which is the case for example when the train is in a tunnel, in urban environment or in a corridor. Main parameters used in the following can be found in Table 4. In particular the range of distances between the TRU and RRU is 100-800 m, where it is shown in [1] that the SNR can be kept at a good level. The subcarrier spacing has been set to 180 kHz, that is compatible with the subcarrier spacing specified in chapter 2.3.3.1 with  $n=6$ . We furthermore consider a carrier frequency of 28 GHz, where a wide amount of spectrum is available for providing high throughput internet access to users.

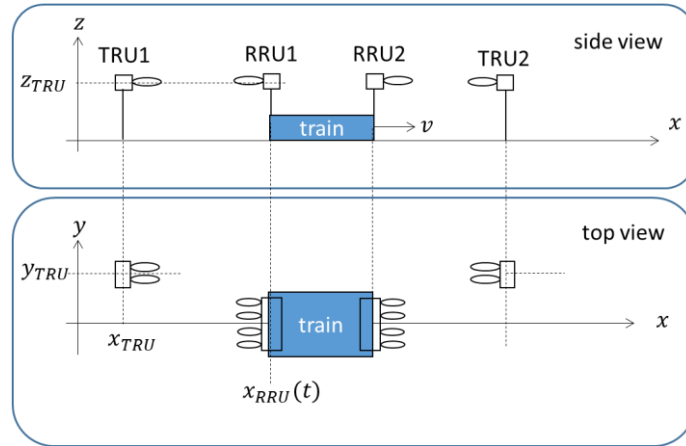


Figure 16. Side view and top view of the scenario.

Table 4. Parameters used in the study.

Parameter	Value
Waveform	OFDM
Carrier spacing	180 kHz
Sampling frequency	184.32 MHz
Carrier Frequency	28 GHz
Transmit antennas	2
Receive antennas	4
$\{x,y,z\}_{TRU}$	$\{0,3,3.5\}$ m
$\{x,y,z\}_{RRU}$	$\{x,0,3.5\}$ m
Distance between TRUs	1000 m
$x_{RRU}$ range	100-800 m

## 4.2 Channel model

The channel has been simulated thanks to the free software Quadriga [20]. Quadriga is a geometry based stochastic channel model that implements several scenarios, among which urban microcell street canyon with LOS has been chosen for this study. Parameters of this channel, such as delay spread, angles of arrival and number of clusters can be found in [21]. Quadriga allows to choose the number of transmit and receive antennas, their azimuth and elevation responses and their spacing. In this study we are considering 2 transmit and 4 receive antennas. The antennas are directive, with  $8^\circ$  aperture, see Figure 17. The optimal antenna spacing is assessed in chapter 4.4.3.



<b>Title:</b>	Deliverable 3.4: Algorithms for backhauling & fronthauling	
<b>Date:</b>	31-05-2017	<b>Status:</b> Final
<b>Security:</b> PU		<b>Version:</b> v1.1

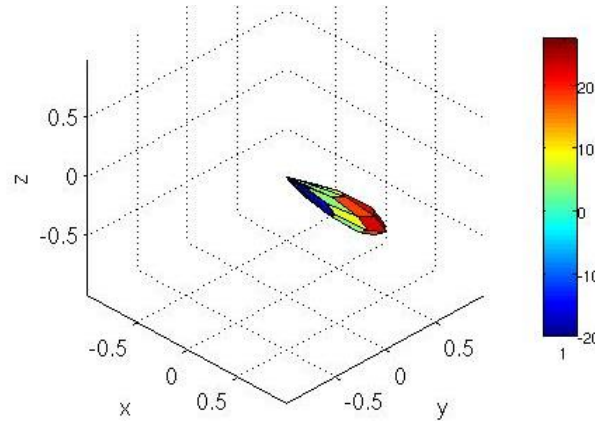


Figure 17. Gain of transmit antenna array element 1 (shown at  $\{x,y,z\}=\{0,0,0\}$ ), in dBi

Quadruga models are available for a large range of frequencies. Here the carrier frequency is 28 GHz.

### 4.3 Doppler modeling and pre-compensation

The Doppler due to the high speed of the RRU is the major impairment in the HST scenario. In this study, Doppler is modeled as a ramp of phase  $\exp(j2\pi\delta(t + \Delta_p))$  for each channel path, with  $\delta$  the actual Doppler and  $\Delta_p$  the delay of path number  $p$ .

Two conditions are met that allow to think that it is possible to pre-compensate the Doppler  $\delta$  at the transmitter:

1. The LOS path is predominant.
2. The distance between the transmitter and the receiver, see Table 4, is high enough for the Doppler to be constant: the Doppler is a function of the cosine of the angle of arrival of the path, and the angle is nearly 0.

In this study, the Doppler is therefore pre-compensated at the transmitter. In our simulations, when Doppler is pre-compensated, a ramp of phase  $\exp(j2\pi\hat{\delta}t)$  is applied on each transmit antenna, with  $\hat{\delta}$  the estimated Doppler,  $\hat{\delta} = \hat{v}/(c/F_c)$ , and  $\hat{v}$  the estimated speed of the receiver. Note that it is out of the scope of this study to estimate the speed  $v$  of the receiver<sup>1</sup>: we chose at the transmitter a value for  $\hat{v}$ , resulting in a residual Doppler  $\delta_{res} \cong |\hat{v} - v|/(c/F_c)$  (it is not an equality, due to the multipath nature of the channel).

### 4.4 MIMO schemes

#### 4.4.1 Spatial Multiplexing

We assess the feasibility of Spatial Multiplexing as described in [19] under the name V-BLAST. This scheme allows to theoretically increase the data rate by a factor of the number of transmit antennas, provided several conditions are met:

<sup>1</sup> It has been shown in the literature that the speed can be estimated very accurately [18][18], especially when it is constant. Errors in the estimation lower than 0.2 m/s are possible.



---

<b>Title:</b>	Deliverable 3.4: Algorithms for backhauling & fronthauling	
<b>Date:</b>	31-05-2017	<b>Status:</b> Final
<b>Security:</b> PU		<b>Version:</b> v1.1

---

- the number of receive antennas is strictly higher than the number of transmit antennas,
- The antennas are decorrelated,
- The channel is more or less frequency selective.
- The SNR is quite high.

The first three conditions ensure that the channel matrix is well-conditioned.

We implemented the ‘Symbol cancellation’ receiver: the symbol transmitted by the antenna with the strongest link is detected first and then subtracted from the received signal before detecting the second symbol: with  $\hat{H}$  (size number of receive antennas  $Nr$  x number of transmit antennas  $Nt$ ) the estimated channel matrix at the receiver, the index  $i_0$  of the first symbol to detect is given by:

$$i_0 = \operatorname{argmin}([\sum_{j=0}^{Nr-1}(|\hat{H}^+(0,j)|^2) \dots \sum_{j=0}^{Nr-1}(|\hat{H}^+(Nt-1,j)|^2)]),$$

where  $\hat{H}^+$  is the pseudo inverse of  $\hat{H}$ . Let then denote  $w_0$  the  $i_0^{th}$  row of  $\hat{H}^+$ . At the receiver, the estimation of the symbol  $s_{i_0}$  transmitted on antenna  $i_0$  is therefore given by  $s_{i_0} = w_0 r_0$  with  $r_0$  the  $Nr \times 1$  received vector. The contribution of  $s_{i_0}$  in the received signal  $r_0$  is then computed by demodulation of  $s_{i_0}$ , modulation and multiplication by the estimated channel matrix. This contribution is subtracted from  $r_0$ , resulting in received signal  $r_1$ . The second transmitted symbol  $s_{i_1}$  is finally detected as  $s_{i_1} = w_1 r_1$  with  $w_1$  the  $i_1^{th}$  row of  $\hat{H}^+$ .

This implementation has been shown [19] to provide better results than Zero Forcing, which consists in (pseudo-)inverting the channel matrix at the receiver to recover the transmitted symbols:  $[s_0 \ s_1]^T = \hat{H}^+ r_0$ .

The algorithm works on a subcarrier basis. It therefore requires an estimation of the  $4 \times 2$  channel on each subcarrier. The estimation of the channel is out of the scope of this study. For feasibility of this estimation at high speeds, the reader is referred to chapter 3.

The throughput that can be achieved with this scheme is shown in Table 5, column three.

#### 4.4.2 Diversity

In order to realize a comparison with the spatial multiplexing scheme presented above, a ‘diversity’ scheme has been implemented, with the same number of antennas. The two transmit antennas transmit the same data. At the receiver, maximum ratio combining is performed using the four receive antennas. The throughput that can be achieved with this scheme is shown in Table 5, column two.

#### 4.4.3 Optimal antenna spacing

Several antenna spacing configurations have been assessed, with 16-QAM 1/2 and residual Doppler=0.03%. Results are presented in Figure 18 and Figure 19. As expected for SM, antennas must be decorrelated and therefore quite far away the one from each other. A spacing  $\Delta Tx$  of transmit antennas and  $\Delta Rx$  of receive antennas of more than 50 times the wave length  $\lambda$  is required. We recall that  $\lambda$  is around 1 cm here. For the diversity scheme, a necessary and sufficient condition for achieving good performance is that  $\Delta Tx$  is small.

In the following we have chosen  $\{\Delta Tx, \Delta Rx\} = \{50\lambda, 50\lambda\}$  for the SM scheme and  $\{\Delta Tx, \Delta Rx\} = \{2\lambda, 2\lambda\}$  for the diversity scheme.

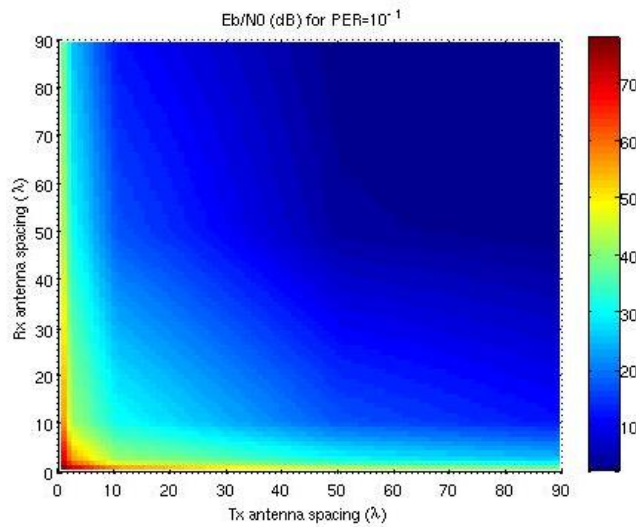


**Figure 18. Assessment of optimal antenna spacing for Spatial Multiplexing**

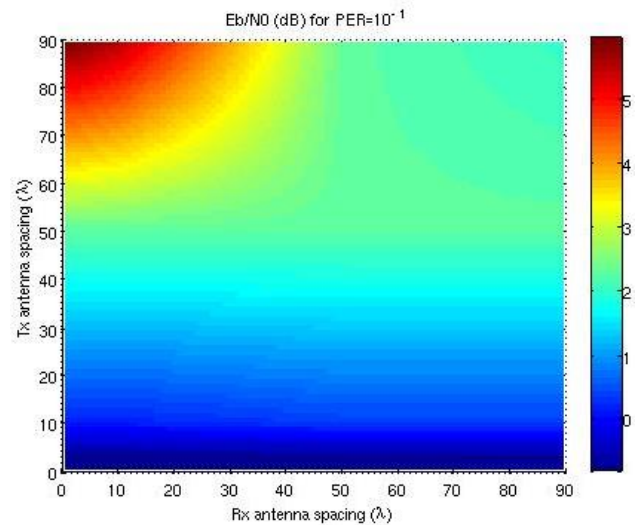


**Figure 19. Assessment of optimal antenna spacing for Diversity**

## 4.5 Simulation results

### 4.5.1 Parameters

The system described in chapter 4.1 has been assessed by means of computer simulations. Several Modulation and Coding Schemes (MCSs) have been implemented: the list can be found in Table 5. In this table the theoretical maximal throughput that can be achieved with each MCS is computed, for Spatial Multiplexing and for Diversity. The color and the marker style associated to each MCS for the simulation curves is given in the most right column.



**Table 5. MCSs assessed and throughput that can be achieved.**

MCS #	MCS		Throughput $\gamma$ , bps/Hz		Plot style	
	Modulation	Rate	Diversity	Spatial mux		
1	QPSK	1/2	1	2	Black	Circle
2		2/3	1.33	2.66		Square
3		3/4	1.5	3		Triangle
4	16-QAM	1/2	2	4	Purple	Circle
5		2/3	2.66	5.33		Square
6		3/4	3	6		Triangle
7	64-QAM	2/3	4	8	Red	Square
8		3/4	4.5	9		Triangle
9	128-QAM	2/3	4.66	9.33	Green	Square
10		3/4	5.25	10.5		Triangle

#### 4.5.2 Residual Doppler 0.03%

On Figure 20 the train speed has been set to 400 km/h and the estimation of the speed at the transmitter to 398 km/h, resulting in a residual Doppler of around 0.03 % of carrier spacing.

For a given MCS, SM allows to double the throughput with respect to Diversity, see Table 5. However, this former MIMO scheme is only efficient in high  $E_b/N_0$  region, as it can be noticed on Figure 20: for example, in order to reach a PER of  $10^{-2}$  with MCS#7, a 8 dB higher  $E_b/N_0$  is required with SM than with Diversity. Nevertheless, the higher the modulation order, the higher the negative impact of the residual Doppler on the PER, due to phase rotations. For this reason, for example, MCS#9 is much more impacted than MCS#7; that's why, going on with this example, for  $E_b/N_0=14$  dB MCS#7 SM has the same performance than MCS#9 Diversity. It must be noted that MCS#7 SM allows a throughput of 8 bps/Hz and MCS#9 Diversity only 4.66 bps/Hz.

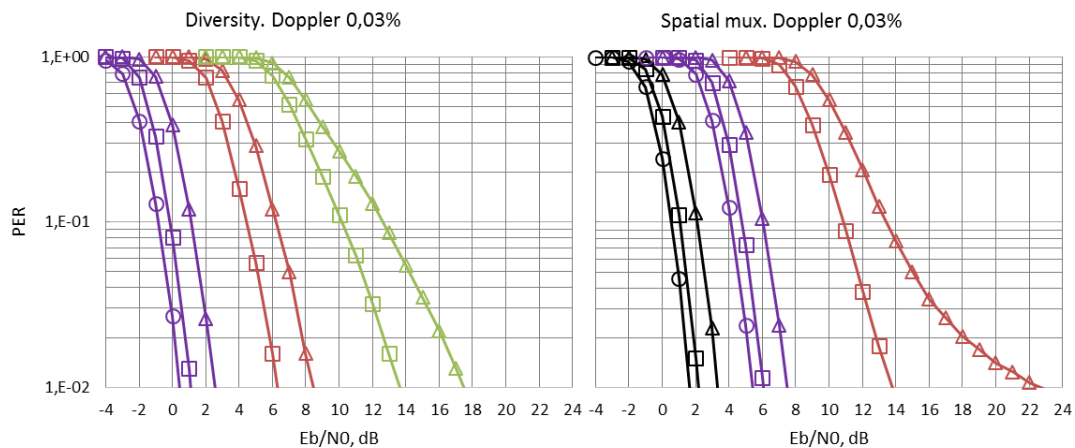


**Figure 20. Packet Error rate of Spatial Multiplexing and Diversity Schemes with 0.03 % residual Doppler. Legend: see Table 5**

In order to quantify the gain provided by SM, Figure 21 plots the throughput that can be achieved by the two schemes, computed as  $\gamma(1-\text{PER})$ , with  $\gamma$  given in Table 5. It is worth noting that the SM scheme achieves a higher throughput than the Diversity scheme from a SNR of 4



dB. For SNR higher than 18 dB (which is possible on the TRU-RRU link according to [17]) SM even allows a throughput 1.8 times higher than Diversity.

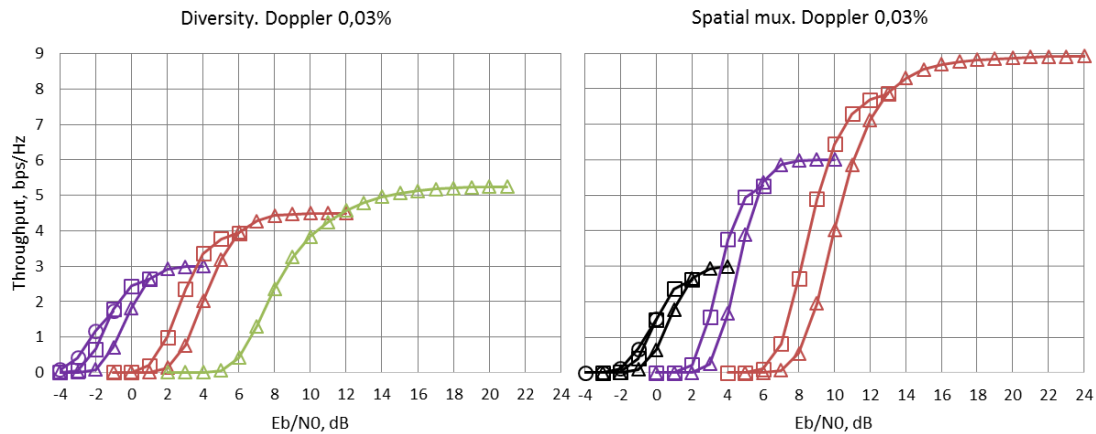


**Figure 21. Throughput of Spatial Multiplexing and Diversity Schemes with 0.03 % residual Doppler. Legend: see Table 5**

#### 4.5.3 Residual Doppler 0.06%

On Figure 22 the train speed has been set to 400 km/h and the estimation of the speed at the transmitter to 396 km/h, resulting in a residual Doppler of around 0.06 % of carrier spacing. In this scenario, the residual Doppler is much more higher than in section 4.5.2, therefore high order modulations are highly impacted. This can be seen on Figure 22 where MCS#7 and higher experience a PER floor. For the same reasons than above, a throughput gain might be expected with SM with respect to Diversity. This is confirmed by Figure 23 that plots the throughput that can be achieved by the two schemes, computed as  $\gamma(1-\text{PER})$ , with  $\gamma$  given in Table 5.

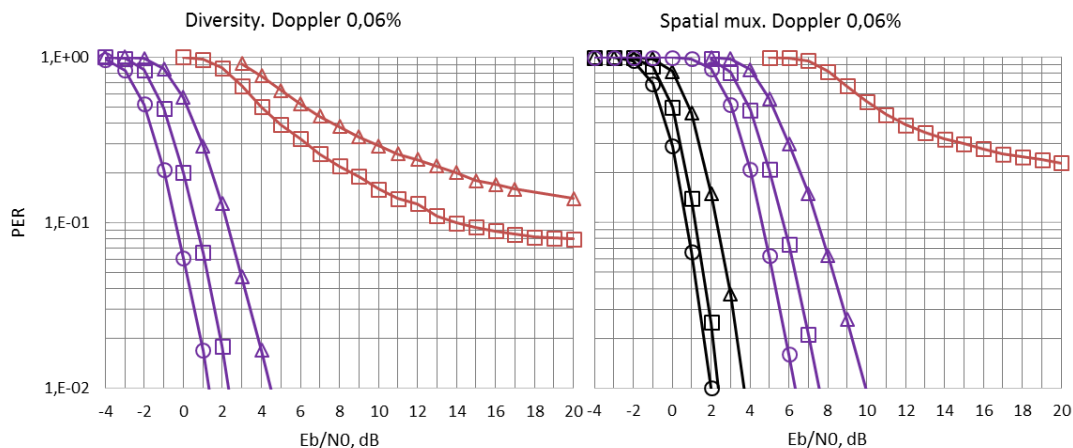


**Figure 22. Packet Error rate of Spatial Multiplexing and Diversity Schemes with 0.06 % residual Doppler. Legend: see Table 5**



It is worth noting that the SM scheme still achieves a higher throughput than the Diversity scheme from a SNR of 4 dB. For SNR higher than 10 dB SM even allows a throughput 1.7 times higher than Diversity.

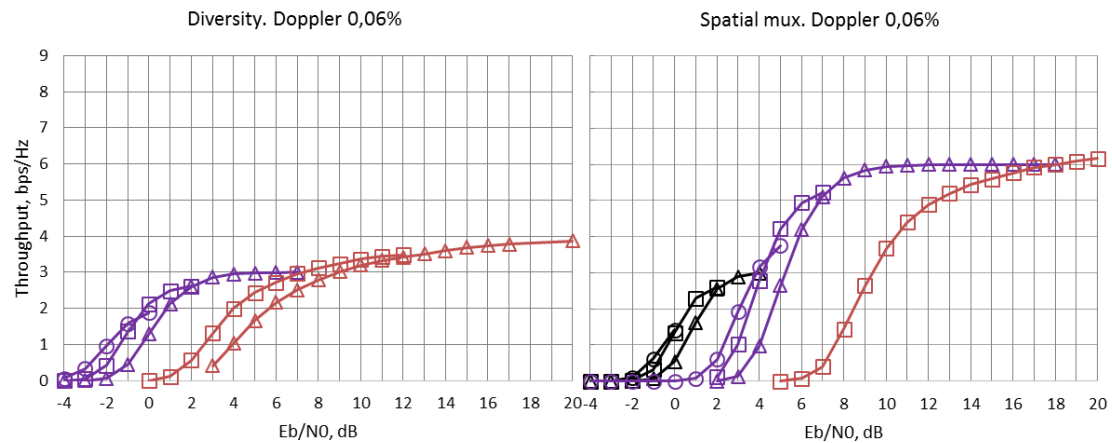


**Figure 23. Throughput of Spatial Multiplexing and Diversity Schemes with 0.06 % residual Doppler. Legend: see Table 5**

## 4.6 Summary

In this study, SM for the backhauling of HST has been assessed. An adequate channel model at 28 GHz carrier frequency has been used to model the highly time variant environment. It has first been shown that in ‘street canyon’ scenario, SM achieves good PER results, only few dBs worse than the Diversity scheme implemented for comparison purpose. It has then been demonstrated that despite the fact that the channel is frequency selective, the LOS path is predominant and therefore the Doppler can be pre-compensated at the transmitter. In case an error on the estimation of the speed is done at the transmitter, more or less Doppler may remain at the receiver. This residual Doppler causes phase rotations that are detrimental to high order modulations. In this situation SM allows to use lower order modulations and is therefore more resistant. SM therefore allows to reach much higher throughputs, around 1.7 times higher than Diversity.

It must nevertheless be noted that the SM scheme presented here requires the estimation at the receiver of  $N_t$  times  $N_r$  channels per carrier, with  $N_t$  (resp.  $N_r$ ) the number of transmit (resp. receive) antennas. The Diversity scheme requires only  $N_r$  channel estimations, that is twice less in our simulations ( $N_t=2$ ). Channel estimation was out of the scope of this study but a study of MIMO fast changing channel estimation can be found in chapter 3. Some more pilots would be required for SM, lowering a little bit the throughput of the scheme.

## 5 Beam alignment techniques

In this chapter we investigate the problem of (multi)-beam alignment for mmW backhaul link established at 28GHz.

We assume that one device has fixed location and is connected to the core network, whereas the other is mobile and serves as moving hot-spot, for instance, in bus or high-speed train.

The information contained in this document is the property of the contractors. It cannot be reproduced or transmitted to thirds without the authorization of the contractors.



---

<b>Title:</b>	Deliverable 3.4: Algorithms for backhauling & fronthauling	
<b>Date:</b>	31-05-2017	<b>Status:</b> Final
<b>Security:</b> PU		<b>Version:</b> v1.1

---

The fixed and the mobile devices are, hereafter, referred to as fixed Terminal radio unit (TRU) and a remote radio unit (RRU), respectively. Both TRU and RRU utilize multiple antennas to establish a directive communication via beamforming. More details of transceiver architecture are described in [22][23].

## 5.1 Transceiver architecture and communication model

The block diagram of the transceiver (identical at TRU and RRU) is depicted in Figure 24. It consists of a base-band unit (BBU) with capability of  $M \times M$  MIMO processing and a DFE that connects the BBU to the RF-FE, which comprises of  $L$  RF beamformers, each one connected to an antenna array of  $N$  elements.

For instance, the mmW transceiver designed in [23] provides 8 digital MIMO channels and 4 RF beamformers which are independently controlled. Two channels are sent/received to/by the same RF beamformer.



**Figure 24: Beamforming at the TRU and RRU**

The communication between transmitter and receiver follows the SF structure proposed in [23]. Our focus is on the initial access procedure, which consists of two phases:

- downlink synchronization**, the RRU detects the synchronization signal (PSS and SSS) and system information transmitted by the TRU in the DL control slot
- beam alignment**, the RRU measures the RSS of the Beam Reference Signal (BRS) to find preferred Tx beam and Rx beam pair(s).

As described in [24], the synchronization and beam reference signals can be transmitted in the same OFDM slot, but over different subcarriers. For instance, in the [24] 18 and 82 resource blocks of the same OFDM symbol are dedicated to synchronization and BRS, respectively. However, the periodicity of PSS and BRS signal is not the same. As a reference, in [24] the PSS is sent with periodicity of 5ms whereas the BRS periodicity can be set either at 5ms or 10ms or 20ms. .

It is assumed that reference signals are beamformed in the RF domain. A beam sweeping strategy is needed to allow the transmission of PSS and BRS to different directions.

In this regard, we distinguish between beam sweep in the time and frequency domains. In the time domain, the RF beam directions are changed in consecutive (localized) or periodic time slots (distributed). In the frequency domain, RF beam directions are fixed but frequency



orthogonality is used to separate reference signals sent for different directions. The report [25] shows, for instance, a possibility for frequency and time domain mapping of BRS.

In this work, we focus on time domain distributed mapping as it can be directly applied to the EU demonstration platform. In fact, as indicated in [26], the EU mmW platform will provide hardware and processing restrictions that do not permit digital beamforming..

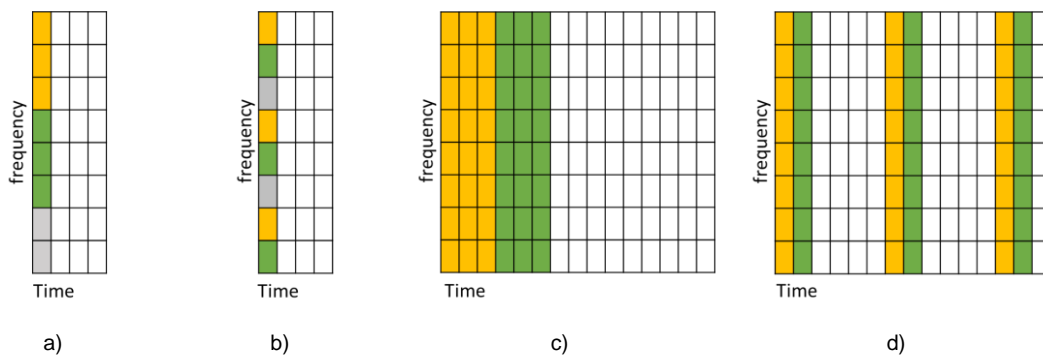


**Figure 25: Reference signal mapping. a) Localized frequency domain, b) Distributed frequency domain, c) Localized time domain and d) Distributed time domain**

## 5.2 Beamforming codebook

In this chapter we describe the analog beamforming codebook that can be utilized in the EU mmW RF transceiver. We focus on codebooks with binary, fixed amplitude and variable phase. More specifically,

- Orthogonal codebook for 3D beamforming:** all antenna elements are active, the beams are narrow with equal maximum array gain and nulls of the  $j$ -th beam correspond to the direction of the maximum gain of any other  $i$ -th beam.
- Hierarchical codebook for 3D beamforming:** antenna elements can be deactivated, the beams are of variable width and nulls of the  $j$ -th beam do not correspond to the direction of the maximum gain of any other  $i$ -th beam

### 5.2.1.1 Orthogonal beamforming codebook

The orthogonal codebook is obtained with a set of orthogonal beamsteering vectors. For instance, for a ULA with  $N$  elements, it is readily obtained via a normalized Discrete Fourier Transform (DFT) matrix with  $N$  columns. Whereas for a URA, it can be computed as 2-dimensional DFT matrix, *i.e.*, as a Kronecker product of two DFT matrices, respectively, with  $N_r$  and  $N_c$  columns where  $N_r$  and  $N_c$  are the number of antenna elements per physical direction.

As illustrated in Figure 26, for each beam the following is true:

- The maximum gain is equal to 1
- The null directions of the  $i$ -th beam correspond to the maximum gain direction of any other  $j$ -th beam



**Title:** Deliverable 3.4: Algorithms for backhauling & fronthauling

**Date:** 31-05-2017

**Status:** Final

**Security:** PU

**Version:** v1.1

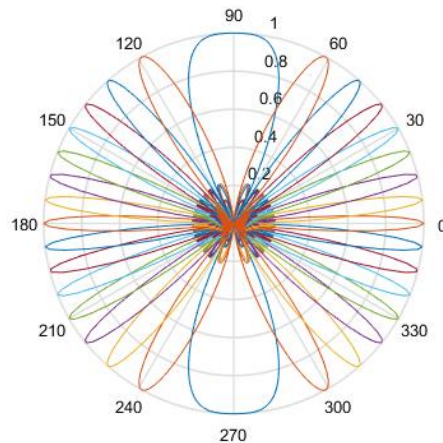


**Figure 26: DFT beamforming codebook**

### 5.2.1.2 Hierarchical codebook with deactivation functionality

The hierarchical codebook is obtained with a combination of beamsteering and antenna selection (activation) techniques. More specifically, the beamforming codebook is organized in levels and in between levels beams have different beamwidths. For instance, in Figure 27, we illustrated an example of hierarchical codebook for a ULA antenna. The whole angular domain, e.g.,  $[-90, 90]$  is first partitioned in  $K$  bins, then for each bin, we design a beamformer such that the HPBW coincides with the upper and lower bounds of the bin. Next, we increase the level, partition each angular bin in  $K$  bins and construct a new set of beamformers.

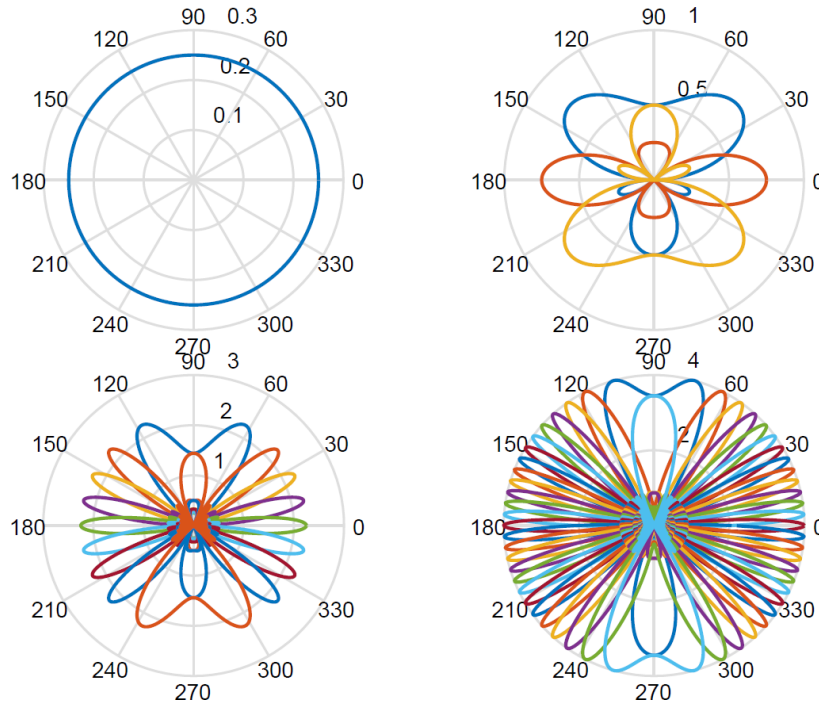


**Figure 27: Hierarchical beamforming codebook**

It results, that  $L = \lceil \log_K(N) \rceil$  partitioning (also referred to as level) are performed and at for the  $l$ -level,  $K^l$  beamformer vectors are defined.

The hierarchical beamformer codebook size is

$$N^b = \sum_{\ell=1}^{\lceil \log_K(N) \rceil} K^\ell = \frac{1 - K^{\lceil \log_K(N) \rceil + 1}}{1 - K} - 1.$$

In order to maximize the SNR per beam, we can alternatively apply the hierarchical codebook construction described in [27] and illustrated in Figure 28. The example shows the codebook with partitioning factor  $K=2$ .

Likewise the orthogonal codebook, the hierarchical codebook for URA can be computed as a Kronecker product of two ULA-type codebooks.

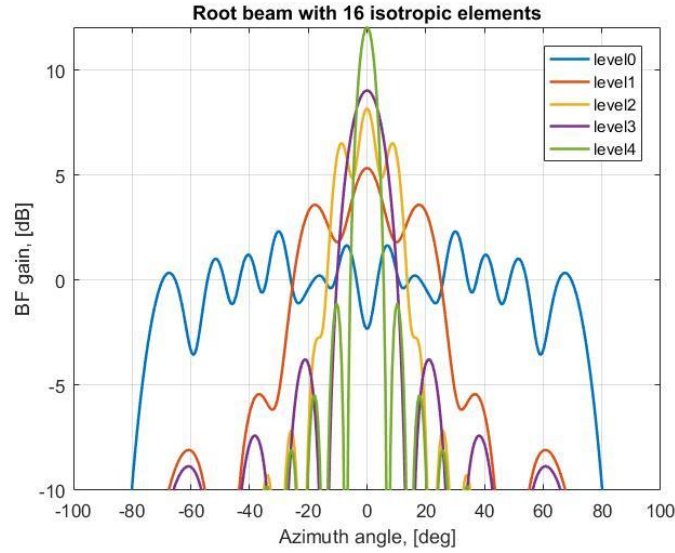


Figure 28: Hierarchical beamforming to maximize the number of active elements

### 5.3 RSS-based strategy for single-path alignment

The algorithm for beam alignment is designed for a time domain, localized mapping of the beams. We assume that the periodicity for the beam alignment phase is fixed and that beam-alignment procedure is prior communication.

Our focus is on the impact of beam alignment overhead on the effective data-rate given by

$$R = \max_{\mathbf{w} \in \mathcal{W}, \mathbf{f} \in \mathcal{F}} B \left( 1 - \frac{T_t}{T_f} \right) \log_2 \left( 1 + \frac{|h|^2 P_{\text{tx}} S(\mathbf{w}, \mathbf{f}, \theta, \phi)}{\sigma^2} \right),$$

where  $T_t$  is the training time,  $T_f$  is the periodicity of beam alignment procedure,  $P_{\text{tx}}$  is the transmit signal power,  $\mathbf{a}_M(\theta)$  and  $\mathbf{a}_N(\theta)$  are the receive and transmit array factor  $S(\mathbf{w}, \mathbf{f}, \theta, \phi) \triangleq |\mathbf{w}^H \mathbf{a}_M(\theta)|^2 |\mathbf{f}^H \mathbf{a}_N(\phi)|^2$ , with  $\mathbf{w}$  and  $\mathbf{f}$  are the receive and transmit beamforming vectors,  $B$  is the signal bandwidth and  $\sigma^2 = N_0 B$  is the noise power over  $B$ .

The effective data-rate, in fact, depends not only on the selected codebook and selected beamforming vectors, but also on the ratio  $T_t/T_f$  which takes into account the overhead for the beam alignment strategy. In the following section, we analyse this metric for an exhaustive and adaptive alignment strategy.

#### 5.3.1 Exhaustive search with orthogonal codebook

Let us assume that TRU and RRU are time aligned and that channel has only one path. The beam alignment procedure with the exhaustive search works as follows:

- the TRU changes beam every  $M$  slots<sup>2</sup>
- the RRU sweeps the RX codebook (see Figure) in  $M$  slots;

<sup>2</sup> Note that for a ULA and orthogonal codebook, the codebook size is equal to the number of antennas.



- the RRU uses measures the RSS power
- the RRU searches the maximum RSS and
- the RRU sends to the TRU the beam state information indicating the slot when the maximum RSS is measured.

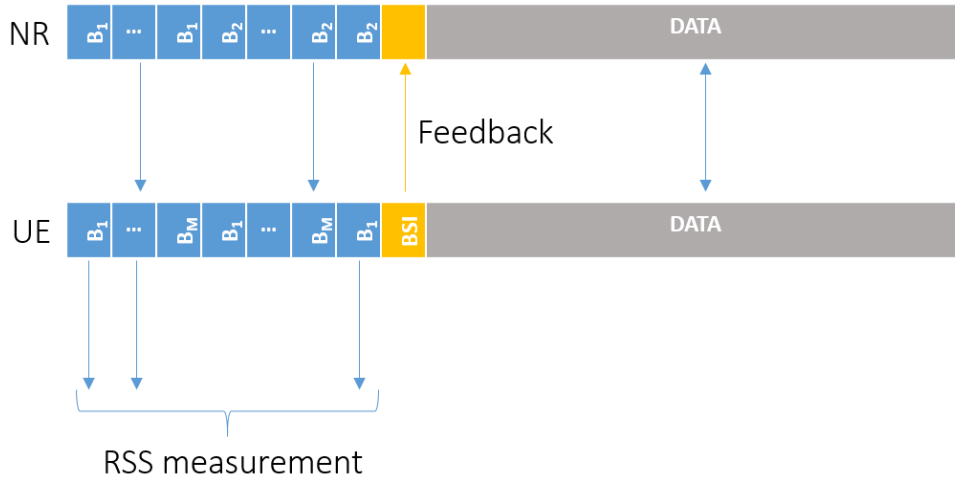


**Figure 29: Training with exhaustive search**

Without loss of generality, consider  $N=M$ . Thus, the training time takes  $N^2$  slots. Also, in an ideal condition, *i.e.*, when both TX and RX beams are perfectly aligned with the channel, the achievable effective rate is given

$$R = B \left( 1 - \frac{(N^2 + 1)}{n} \right) \log_2 (1 + \text{SNR}_0 N^2), \tag{1}$$

$$\approx 2B \left( 1 - \frac{N^2}{n} \right) \log_2 (\text{SNR}_0 N),$$

where  $n$  is the length of the training periodicity in number of slots and  $\text{SNR}_0 \triangleq |h|^2 P_{\text{tx}} / \sigma^2$  represent the SNR obtained without array gain.

We notice that, on the one hand, the rate reduces with  $N^2$  due to the overhead and, on the other hand, it increases with  $\log(N)$ . Thus, we expect a trade-off between rate and overhead training. This trade-off, in fact, can be obtained by computing the maximum of (3) with respect to  $N$  (indicated as a variable  $x$  in the following equation). It yields

$$\frac{\partial R(x; \text{SNR}_0)}{\partial x} = 0 \tag{2}$$

and

$$x = n - 1 - \frac{(1 + \text{SNR}_0 x)}{\text{SNR}_0} \ln (1 + \text{SNR}_0 x) \tag{3}$$

Subsequently, the optimum training length is given by

$$T_t = \lceil x_{\text{opt}} \rceil T_{\text{sym}} \tag{4}$$



where  $x_{opt}$  is the solution of (5). The Figure 30 shows, for instance, the optimum overhead ratio as function of  $T_f$  with  $T_{sym} = 1/\Delta f$ . We remark also the dependency with  $SNR_0$ , and the lower the  $SNR_0$ , the higher the training overhead is.

To give a concrete example, for instance, we can assume  $T_f=10$  ms,  $SNR_0=20$  dB,  $T_{sym}=14.3$   $\mu$ s. From the curve, it results that the optimum overhead is 0.1, which yields  $0.1 T_f / T_{sym} = 70$  slots.

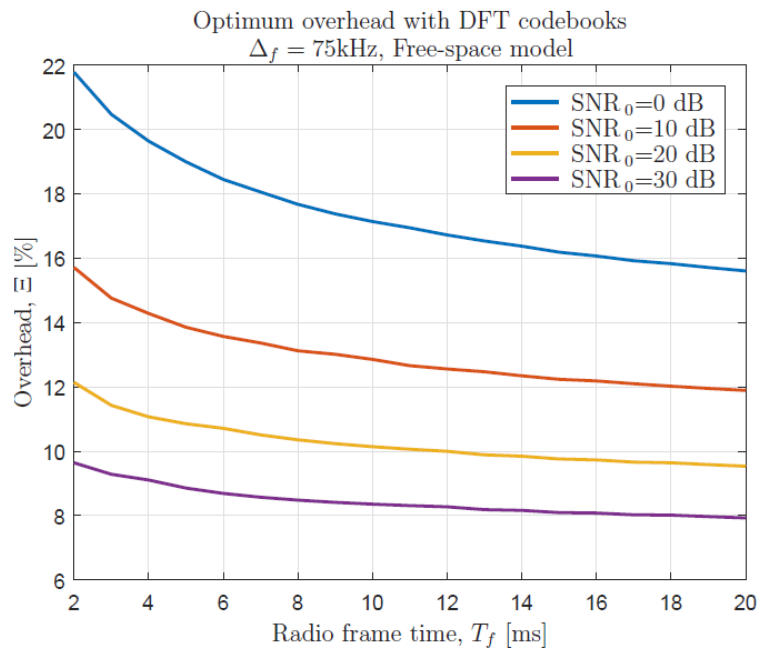


Figure 30: Optimum overhead with exhaustive search

### 5.3.2 Adaptive search with hierarchical codebook

Also in this case, let us assume that TRU and RRU are time aligned and that channel has only one path. The adaptive beam alignment procedure with hierarchical codebook works as follows:

- The TRU and RRU start with an exhaustive search mechanism using the  $K$  beamformers of level-1.
- For each beam-pair, both TRU and RRU measure the RSS of the reference signal
- TRU and RRU select, independently, the  $k$ th direction with maximum SNR
- TRU and RRU perform a new partition of the angular sector covered by the selected beam and compute  $K$  new beamformers
- Iterate the whole process until the narrowest beam are formed

Following the same steps in the previous Section, we compute the maximum effective rate



$$R = B \left( 1 - \frac{(K^2+1)\lceil \log_K(N) \rceil}{n} \right) \log_2 (1 + \text{SNR}_0 N^2),$$

$$\approx 2B \left( 1 - \frac{(K^2+1)\lceil \log_K(N) \rceil}{n} \right) \log_2 (\text{SNR}_0 N).$$

In contrast to the exhaustive search with orthogonal codebook, we notice

- $T_t \in \mathcal{O}(\log_K(N))$ , this indicates that the beamtraining overhead increase with  $N$ , but sublinearly
- $T_t \in o(N^2)$ , this shows that the hierarchical search is much more time-efficient than the exhaustive search and,
- $T_t(N) < \log_2(\text{SNR}_0 N)$ , this demonstrates that in this search method, the array gain is the dominant factor for a rate increase. Thus by increasing  $N$ , the rate grows despite of a longer training time for a sufficiently large  $\text{SNR}_0$ .

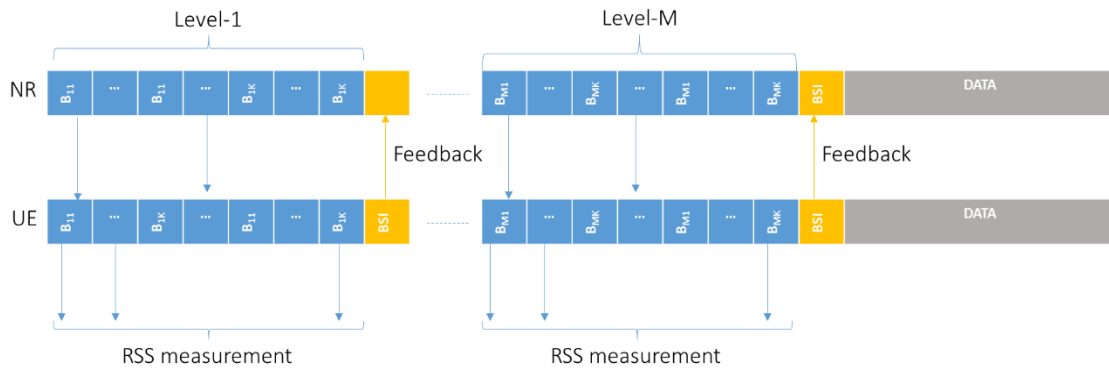


**Figure 31 : Training with adaptive search**

### 5.3.3 Performance comparison between exhaustive and adaptive search strategies

Next, we study the impact of the different search strategies as well as the codebook size on the effective data-rate. We focus on an ideal MIMO-OFDM communication system with



**Title:** Deliverable 3.4: Algorithms for backhauling & fronthauling  
**Date:** 31-05-2017 **Status:** Final  
**Security:** PU **Version:** v1.1

Parameter	Value
Waveform	OFDM
Carrier spacing	75 kHz
Sampling frequency	153.6 MHz
Carrier Frequency	28 GHz
TX power	30dBm
SNR <sub>0</sub>	{0,20} dB
RF beamformer	1
Number of TX antenna	{8,32}
Number of RF antenna	{8,32}
Antenna type	ULA
$\theta, \phi$	{0,20} deg

**Table 6 :Simulation parameter for beamtraining comparison**

Figure 32 shows the achievable rate as a function of the beam alignment periodicity with the exhaustive and hierarchical training strategies.

First, we observe that, for exhaustive search (blue lines), there is a crossing point between the rate performance achieved with N=8 (solid line) and N=32 (dashed line). This value is around 55ms, and it is related to the high overhead for N=32. In fact, if the periodicity of the beam alignment procedure is not long enough, several slots are used for training and the SNR gain achieved with larger antenna array is not sufficient to compensate the time inefficiency of the protocol.

In contrast, with the adaptive search and hierarchical codebook (red lines) the highest rate is achieved with N=32 despite of the frame length.

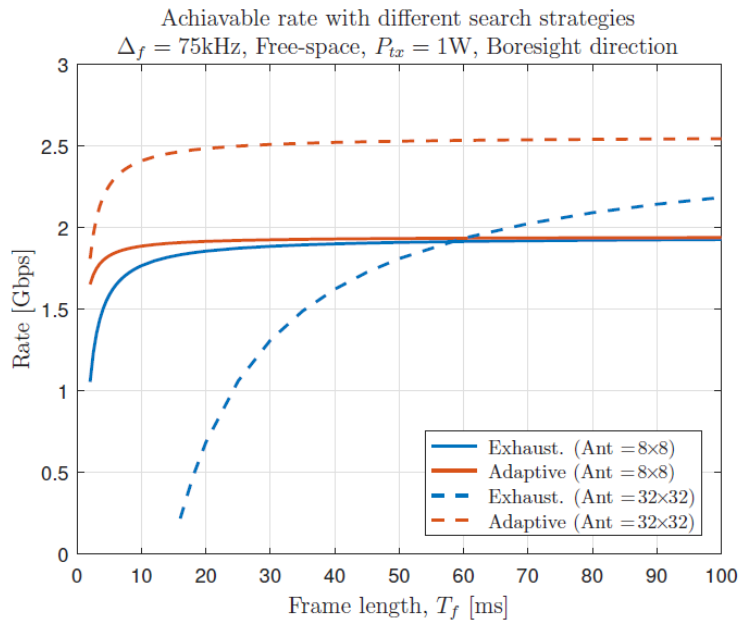


**Figure 32: Achievable rate as a function of the beamtraining periodicity (frame length)**

The next result concerns the problem of beam misalignment and, more specifically, we evaluate the effective rate as a function of the training time (obtained by varying the number of antennas) by changing the location of the receiver.

First, we simulate an increase of the distance between TRU and RRU by varying the  $\text{SNR}_0$ . In Figure 33 it can be noticed the exhaustive search strategy has an optimum training time (which can be determined analytically) whereas the rate achieved with hierarchical search grows despite the increase of the training period. We also notice that the location of the maximum rate for the exhaustive search changes with the  $\text{SNR}_0$ , and it increases when the SNR decreases. This indicates that, just like power control, there is a “training control” mechanism to be devised.

Finally, we vary the location of the RRU by changing the angle of arrival and departure. From Figure 34, it can be noticed that the rate obtained with the exhaustive search is also a function of the angle and oscillates based upon the choice of  $T_b$ , as the latter depends on  $N$ , thus on the beamformers in the codebook.

This phenomenon is not visible with the hierarchical search as the codebook is denser in the angular domain.

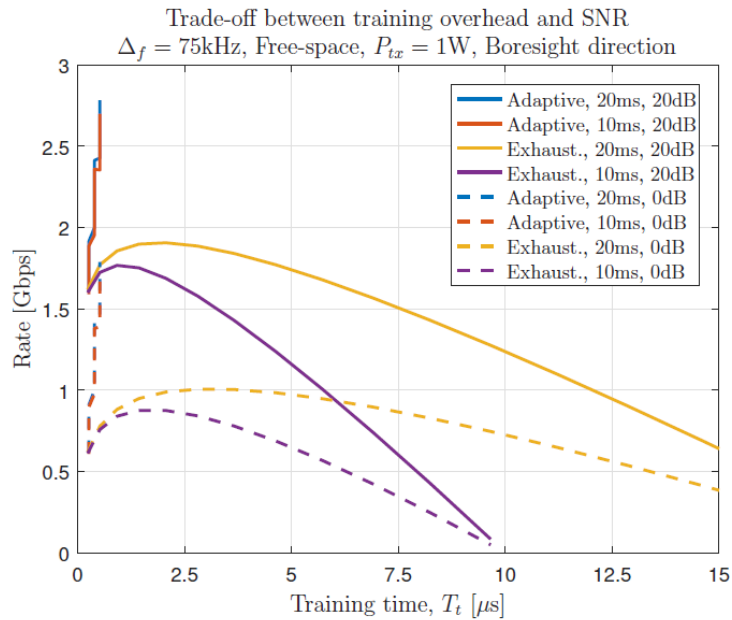


Figure 33 : Achievable rate as a function of the training time and SNR

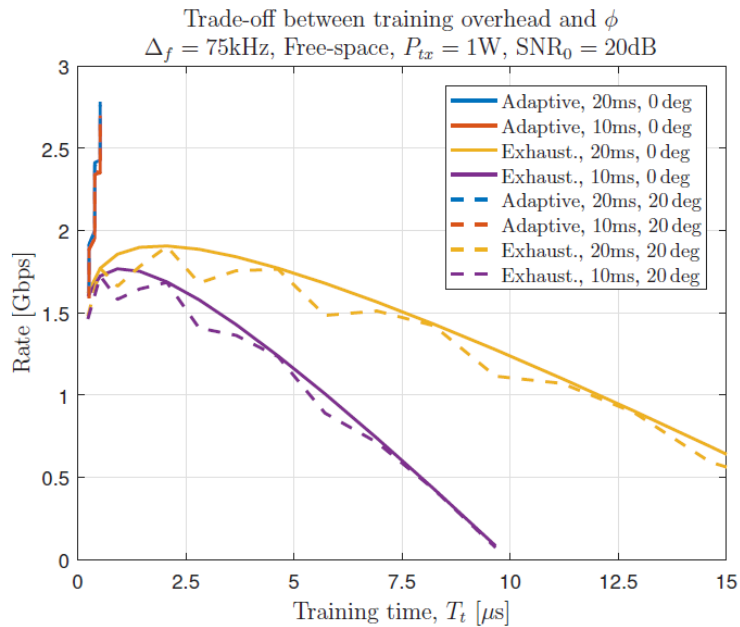


Figure 34 : Achievable rate as a function of the training time and location



**Title:** Deliverable 3.4: Algorithms for backhauling & fronthauling  
**Date:** 31-05-2017      **Status:** Final  
**Security:** PU      **Version:** v1.1

---

## 5.4 Summary

In this chapter we investigated the impact on data rate of two beamsearching strategies widely considered in pre-5G standardization. The focus was on a localized time domain mapping of the reference signal as it will be applied in the EU mmW transceiver implementation. It was found that for exhaustive search methods an optimum length of the training time exists and it depends on the periodicity of the alignment procedure as well as location. Whereas for a training procedure based on adaptive search, the longer the training is (i.e., the higher the hierarchical level is) the higher the rate is. This leads to the conclusion that hierarchical search is more time and rate efficient.



---

<b>Title:</b>	Deliverable 3.4: Algorithms for backhauling & fronthauling	
<b>Date:</b>	31-05-2017	<b>Status:</b> Final
<b>Security:</b> PU		<b>Version:</b> v1.1

---

## 6 Conclusion

In this deliverable, technologies have been presented for supporting very high bit rate services in high mobility. First, in chapter 2, possible candidates for the 3GPP 5G NR numerology including subcarrier spacing, CP length, FFT size, and subframe length in a 30 GHz carrier frequency band have been proposed. It has been shown through extensive computer simulations that in a HST environment, using larger subcarrier spacing values of at least 120 kHz would be beneficial in terms of BLER and spectrum efficiency performances. DMRS design has then been conducted, in chapter 3, so as to find the best trade-off between the channel estimation accuracy improvement and overhead reduction, considering severe Doppler effect of the HST scenario. Link level simulations proved that in a HST environment, using frequency-domain sparse and time-domain dense DMRS allocation would be beneficial in terms of BLER and spectrum efficiency performances. In chapter 4, multiple antenna systems have been assessed for throughput increase of the backhaul link of HST. Considering Doppler and accurate channel modeling, it has been shown that spatial multiplexing with Doppler pre-compensation is possible. This scheme allows for a throughput gain in the order of 50%. Nevertheless this algorithm requires a pilot overhead for estimation of the MIMO channel. Finally, in chapter 5, the impact on data rate of two beamsearching strategies widely considered in pre-5G standardization have been investigated. Two conclusions are drawn depending on the nature of the beam search: exhaustive or adaptive. For the former one an optimum length of the training time exists whereas for the latter one the longer the training the higher is the rate. Hierarchical searches are therefore more time and rate efficient.



---

<b>Title:</b>	Deliverable 3.4: Algorithms for backhauling & fronthauling	
<b>Date:</b>	31-05-2017	<b>Status:</b> Final
<b>Security:</b> PU		<b>Version:</b> v1.1

---

## References

- [1] 3GPP TR 38.913, "Study on scenarios and requirements for next generation access technologies," v. 0.4.0, Jun. 2016.
- [2] 3GPP TR 38.802, "Study on new radio NR access technology; physical layer aspects," v. 0.1.0, Aug. 2016.
- [3] S. Choi et al., "Mobile hotspot network system for high-speed railway communication using millimeter waves," *ETRI Journal*, vol. 38, no. 6, pp. 1052-1063, Dec. 2016.
- [4] M. R. Akdeniz et al., "Millimeter wave channel modeling and cellular capacity evaluation," *IEEE J. Sel. Areas Commun.*, vol. 32, no. 6, pp. 1164–1179, Jun. 2014.
- [5] T. S. Rappaport et al., "Broadband millimeter-wave propagation measurements and models using adaptive-beam antennas for outdoor urban cellular communications," *IEEE Trans. Antennas Propag.*, vol. 61, no. 4, pp. 1850–1859, Apr. 2013.
- [6] 3GPP TR 38.900, "Channel model for frequency spectrum above 6 GHz," v. 1.0.1, Jun. 2016.
- [7] J. G. Proakis and M. Salehi, *Digital Communications*, 5th ed. New York, NY: McGraw-Hill, 2008.
- [8] S. Herbert et al., "Characterizing the spectral properties and time variation of the in-vehicle wireless communication channel," *IEEE Trans. Commun.*, vol. 62, no. 7, pp. 2390–2399, Jul. 2014.
- [9] A. G. Armada, "Understanding the effects of phase noise in orthogonal frequency division multiplexing (OFDM)," *IEEE Trans. Broadcast.*, vol. 47, no. 2, pp. 153–159, Jun. 2001.
- [10] L. X. Cai et al., "Rex: A randomized EXclusive region based scheduling scheme for mmWave WPANs with directional antenna," *IEEE Trans. Wireless Commun.*, vol. 9, no. 1, pp. 113–121, Jan. 2010.
- [11] 3GPP, "WF on phase noise modeling," R1-165685, May 2016.
- [12] 3GPP, "Phase noise model for above 6 GHz," R1-166041, May 2016.
- [13] 3GPP, "Discussion on phase noise modeling," R1-163984, May 2016.
- [14] ICT-671650 mmMAGIC project, "Initial multi-node and antenna transmitter and receiver architectures and schemes," Deliverable D5.1, Mar. 2016. [Online]. Available: [https://bscw.5gmmagic.eu/pub/bscw.cgi/d95056/mmMAGIC\\_D5\\_1.pdf](https://bscw.5gmmagic.eu/pub/bscw.cgi/d95056/mmMAGIC_D5_1.pdf)
- [15] 3GPP, "Final report of 3GPP TSG RAN1 #85," R1-166056, May 2016.
- [16] 3GPP, "WF on CDL-D model for high speed train scenario at 30GHz for RRH and relay," R1-168174, Aug. 2016.
- [17] Sung-Woo Choi, Heesang Chung, Junhyeong Kim, Jaemin Ahn, and Ilgyu Kim, "Mobile Hotspot Network System for High-Speed Railway Communications Using Millimeter Waves," *ETRI Journal*, vol. 38, no. 6, Dec. 2016, pp. 1052-1063
- [18] Malvezzi, M., Vettori, G., Allotta, B., Pugi, L., Ridolfi, A., Cuppini, F., & Salotti, F. (2011, May). Train position and speed estimation by integration of odometers and IMUs. In 9th World Congress on Railway Research, Lille, France (pp. 22-26).
- [19] P. Wolniansky et al., "V-BLAST: An architecture for realizing very high data rates over the rich-scattering wireless channel," In *Signals, Systems, and Electronics, 1998. ISSSE 98. 1998 URSI International Symposium on* (pp. 295-300). IEEE.
- [20] S. Jaeckel et al., "Quadriga: A 3-d multi-cell channel model with time evolution for enabling virtual field trials," *IEEE Transactions on Antennas and Propagation*, 62(6), 3242-3256.



---

**Title:** Deliverable 3.4: Algorithms for backhauling & fronthauling  
**Date:** 31-05-2017      **Status:** Final  
**Security:** PU      **Version:** v1.1

---

- [21] M. Peter et al., " Measurement Campaigns and Initial Channel Models for Preferred Suitable Frequency Ranges," Deliverable D2.1 the mmMAGIC project, March 2016, [online] Available: <https://5g-mmmagic.eu/results/#deliverables>
- [22] Saila Tammelin et al., "Front-end design," 5GCHAMPION D3.1
- [23] Wouter Tavernier et al., "5G CHAMPION architecture, API- and interface document," 5GCHAMPION D2.1
- [24] Verizon 5G TF; Air Interface Working Group; Verizon 5th Generation Radio Access; Physical channels and modulation (Release 1), 10/2016
- [25] Intel, "Beam management for initial and candidate beam discovery", 3GPP R1-1609516, 10/2016
- [26] "mmWave backhauling & fronthauling platform," 5GCHAMPION D3.5
- [27] Z. Xiao, T. He, P. Xia and X. G. Xia, "Hierarchical Codebook Design for Beamforming Training in Millimeter-Wave Communication," in IEEE Transactions on Wireless Communications, vol. 15, no. 5, pp. 3380-3392, May 2016.